

HRAS-driven cancer cells are vulnerable to TRPML1 inhibition

Jewon Jung¹, Kwang-Jin Cho², Ali K Naji³, Kristen N Clemons^{1,4}, Ching On Wong¹, Mariana Villanueva^{5,6}, Steven Gregory^{1,4}, Nicholas E Karagas^{1,4}, Lingxiao Tan^{1,4}, Hong Liang¹, Morgan A Rousseau¹, Kelly M Tomasevich¹, Andrew G Sikora^{5,6}, Ilya Levental^{1,4}, Dharini van der Hoeven³, Yong Zhou^{1,4}, John F Hancock^{1,4} & Kartik Venkatachalam^{1,4,*} 

Abstract

By serving as intermediaries between cellular metabolism and the bioenergetic demands of proliferation, endolysosomes allow cancer cells to thrive under normally detrimental conditions. Here, we show that an endolysosomal TRP channel, TRPML1, is necessary for the proliferation of cancer cells that bear activating mutations in *HRAS*. Expression of *MCOLN1*, which encodes TRPML1, is significantly elevated in *HRAS*-positive tumors and inversely correlated with patient prognosis. Concordantly, *MCOLN1* knockdown or TRPML1 inhibition selectively reduces the proliferation of cancer cells that express oncogenic, but not wild-type, *HRAS*. Mechanistically, TRPML1 maintains oncogenic *HRAS* in signaling-competent nanoclusters at the plasma membrane by mediating cholesterol de-esterification and transport. TRPML1 inhibition disrupts the distribution and levels of cholesterol and thereby attenuates *HRAS* nanoclustering and plasma membrane abundance, ERK phosphorylation, and cell proliferation. These findings reveal a selective vulnerability of *HRAS*-driven cancers to TRPML1 inhibition, which may be leveraged as an actionable therapeutic strategy.

Keywords cancer; cholesterol; endolysosomes; *HRAS*; TRPML1

Subject Categories Cancer; Membrane & Intracellular Transport; Signal Transduction

DOI 10.15252/embr.201846685 | Received 3 July 2018 | Revised 28 January 2019 | Accepted 1 February 2019

EMBO Reports (2019) e46685

Introduction

Mutated *RAS* oncogenes, which represent leading causes of cancer [1], encode constitutively active small G proteins that are currently beyond the reach of direct pharmacological inhibition. Although

inhibition of downstream effectors—BRAF, MEK, or ERK—has been met with some success, efficacy of these strategies is limited by factors such as ubiquity of MEK–ERK signaling, propensity for acquired resistance, and myriad feedback loops associated with unremitting *RAS* activity [1]. Pharmacological inhibition of BRAF, for example, induces paradoxical activation of *RAS*–ERK signaling and the undesirable potentiation of cell proliferation [2]. Alternatively, development of resistance to RAF or MEK inhibition due to somatic mutations and/or gene amplifications can reinstate ERK activation and tumorigenesis [3].

An approach to overcome these obstacles involves the identification and disruption of ancillary cellular processes that are selectively upregulated in *RAS*-driven cancers. This strategy may reveal potential vulnerabilities that can be exploited to mitigate oncogenesis. For example, molecular mechanisms that permit cancer-specific reorganization of cellular metabolism constitute pathways that could be targeted to deter tumorigenesis with exquisite sensitivity and specificity [4–6]. In this context, components of the autophagic and endolysosomal system represent actionable targets [7–11]. Indeed, arresting autophagy and lysosomal degradation via dissipation of the endolysosomal pH gradient using chloroquine is beneficial in some preclinical cancer models, although it is not clear whether the sensitivity to chloroquine correlates with *RAS* mutations [12,13].

In order to prevent unintended potential side effects of blanketed endolysosomal ablation, we reasoned that a cogent strategy to mitigate tumorigenesis would involve the prior determination of the endolysosomal proteins that contribute to disease. To this end, we examined the patterns of endolysosomal gene expression in *HRAS*-driven tumors. We found that tumors with oncogenic *HRAS* mutations exhibit a gene expression signature that reflects increased endolysosomal biogenesis via the *Mitf*/*Tfe3*/*Tfeb*-family of transcription factors [14–17]. Importantly, the gene encoding an endolysosomal cation channel, *MCOLN1*, was a core element of this transcriptional program. We found that oncogenic *HRAS*-expressing

1 Department of Integrative Biology and Pharmacology, McGovern Medical School, the University of Texas Health Sciences Center (UTHealth), Houston, TX, USA

2 Department of Biochemistry and Molecular Biology, Boonshoft School of Medicine, Wright State University, Dayton, OH, USA

3 Department of Diagnostic and Biomedical Sciences, School of Dentistry, The University of Texas Health Science Center, Houston, TX, USA

4 Graduate Program in Biochemistry and Cell Biology, MD Anderson Cancer Center, UTHealth Graduate School of Biomedical Sciences, Houston, TX, USA

5 Bobby R. Alford Department of Otolaryngology-Head and Neck Surgery, Baylor College of Medicine, Houston, TX, USA

6 Patient Derived Xenografts and Advanced *in vivo* Models Core Facility, Baylor College of Medicine, Houston, TX, USA

*Corresponding author. Tel: +1 713 500 7504; E-mail: Kartik.venkatachalam@uth.tmc.edu

cancer cells were vulnerable to TRPML1 inhibition or *MCOLN1* knockdown. Investigation of the underlying mechanisms revealed a role for TRPML1 in the maintenance of plasma membrane cholesterol levels. The mislocalization of plasma membrane cholesterol following inhibition of TRPML1 deterred $HRAS^{G12V}$ -driven ERK activation. These studies underscore the utility of a systems approach to identify disease-specific endolysosomal proteins, and raise the possibility that targeting the function of TRPML1 could limit the growth of cancers driven by oncogenic *HRAS*.

Results

The endolysosomal gene expression signature in tumors bearing oncogenic *HRAS* mutations suggests a role for *MCOLN1*

Cancers of the bladder, head and neck region, and thyroid exhibit a propensity for activating mutations in *HRAS* [18–20]. Our examination of TCGA datasets revealed that cancers with the highest fraction of *HRAS* mutations at codons 12, 13, 61, and 117 were bladder urothelial carcinoma (BLCA), head and neck squamous cell carcinoma (HNSC), and thyroid carcinoma (THCA) (~60% of patients with oncogenic *HRAS* mutations presented with one of these 3 diseases). We asked whether gene expression patterns indicative of endolysosomal biogenesis are apparent in these *HRAS*-driven tumors. We focused our attention on 210 genes that encode a broad spectrum of endolysosomal proteins including hydrolytic enzymes, subunits of the V-ATPase complex, ion channels, transporters, regulators of vesicle trafficking, and components of autophagy/mTOR-related metabolic processes. RNA-seq analyses of HNSC, BLCA, and THCA tumors and matched normal tissues revealed a gene expression signature comprised of 72 significantly upregulated genes, 61 significantly downregulated genes, and 77 genes whose expression did not change significantly (Fig 1A). Upregulated genes included *MCOLN1*, which encodes a $PI(3,5)P_2$ -activated endolysosomal Ca^{2+} channel called TRPML1 [21]. Also upregulated was *VAC14*, whose protein product is part of an enzyme complex required for $PI(3,5)P_2$

synthesis (Fig 1A, *inset*) [21,22]. Mirroring the increase in *VAC14* expression, expression of *MTM1*, which encodes a lipid phosphatase that breaks down $PI(3,5)P_2$ (Fig 1A, *inset*) [23], was decreased in *HRAS* tumors (Fig 1A; yellow circle). Thus, *HRAS* transformed tumors demonstrate a juxtaposition of elevated *MCOLN1* expression and a possible shift in the dynamics of $PI(3)P$ – $PI(3,5)P_2$ inter-conversion toward synthesis of $PI(3,5)P_2$ —the endosomal phosphoinositide that activates TRPML1.

Analysis of endolysosomal gene expression reveals underlying regulatory mechanisms and implicates *MCOLN1* as an actionable hub in *HRAS* tumors

Unsupervised hierarchical clustering of the pairwise correlations of gene expression revealed four major clusters of coregulated genes (Fig 1B and Appendix Fig S1). Average Z-scores indicated increased expression of genes belonging to clusters 1 and 3 and repression of genes belonging to cluster 4 (Fig 1C). *VAC14* and *MCOLN1* belonged to clusters 1 and 3, respectively, whereas *MTM1* belonged to cluster 4. These data suggest coordinated patterns of endolysosomal gene expression in tumors bearing oncogenic mutations in *HRAS*. This insight led us to focus on the Mitf/Tfe3/Tfeb transcription factors, which drive *en masse* expression of endolysosomal genes that belong to the “Coordinated Lysosomal Expression and Regulation” (CLEAR) family [14–17]. Gene set enrichment analysis (GSEA) [24] of the endolysosomal gene expression signature revealed enriched expression of CLEAR targets in *HRAS*-driven tumors (Fig 1D). In agreement with these bioinformatic analyses, RT-qPCR revealed that expression of *MITF*, *TFE3*, and *TFE3* is elevated in oncogenic *HRAS*-positive HN31 oral cancer cells [25] in comparison with HN31 cells stably expressing an shRNA against *HRAS* (Fig 1E). Using previously validated antibodies [26], we found that protein levels of Tfeb were also elevated in HN31 cells compared to the variants stably expressing *HRAS* shRNA (Fig 1F). Furthermore, expression of the CLEAR target genes—*MCOLN1*, *CTSA*, *CTSD*, *VAC14*, *LAMP1*, and *GBA*—was significantly elevated in an *HRAS*-dependent manner (Fig 1G). Concordantly, knockdown of *MITF* or *TFEB* decreased the

Figure 1. BLCA, HNSC, and THCA tumors bearing oncogenic *HRAS* mutations exhibit upregulation of the CLEAR endolysosomal gene network.

- Plot showing the average Z-scores of 210 endolysosomal genes plotted against the negative \log_{10} of the P-values from the one-sample t-test of whether average Z-score $\neq 0$. Green circles represent significantly upregulated genes ($Z > 0$ and $P < 0.05$). Magenta circles represent significantly downregulated genes ($Z < 0$ and $P < 0.05$). Gray circles represent genes whose expression is not significantly changed ($P > 0.05$). All comparisons were between cancers and normal cells from the same tissue. Dashed line shows position on y-axis that corresponds to $P = 0.05$. Positions of *MCOLN1* (red circle), *VAC14* (blue circle), and *MTM1* (yellow circle) are indicated. *Inset*, schematic showing that *Mtm1* and *Vac14* regulate the levels of $PI(3,5)P_2$ and, thereby, influence TRPML1 activity.
- Unsupervised hierarchical clustering of Pearson's coefficients of pairwise correlation of gene expression reveals 4 indicated clusters.
- Violin plots of average Z-scores of genes that belong to the four clusters derived from hierarchical clustering. The thick horizontal dashed lines in each sample set represent median; thin dashed lines represent the quartiles; polygons represent density estimates of data and extend to extreme values. Statistical tests employed were 1-sample t-test or Wilcoxon signed rank test to examine significance of differences from a hypothetical value of 0.
- GSEA conducted on endolysosomal genes ranked on the basis of increasing Z-scores. Positions of the CLEAR target genes are indicated.
- Bar graph showing the relative expression of the indicated genes in the indicated cell types. Values were normalized to respective “HN31 + *HRAS* shRNA” average and represent mean \pm SEM. Data points represent values from biological replicates. Statistical test employed was Student's t-test.
- Western blots performed on extracts isolated from the indicated cells probed with antibodies against Tfeb and tubulin. Molecular weights are shown on the left. Bar graph shows relative Tfeb levels in the indicated samples. Values were normalized to “HN31 + *HRAS* shRNA” and represent mean \pm SEM. Data points represent values from biological replicates. Statistical test employed was Student's t-test.
- Bar graph showing the relative expression of the indicated genes in the indicated cell types. Values were normalized to respective “HN31 + *HRAS* shRNA” average and represent mean \pm SEM. Data points represent values from biological replicates. Statistical test employed was Student's t-test.
- “Attribute circle layout” generated from Pearson's coefficients of pairwise correlation of gene expression using Cytoscape. Decreasing node size (clockwise from *MCOLN1*) reflects decreasing closeness centrality; node color represents degree (number of directed edges); edge color represents Pearson's correlations.
- Bar graph showing the relative expression of *MCOLN1* in the indicated cell types. Values were normalized to HT1197 average and represent mean \pm SEM. Data points represent values from biological replicates. Statistical test employed was Student's t-test.

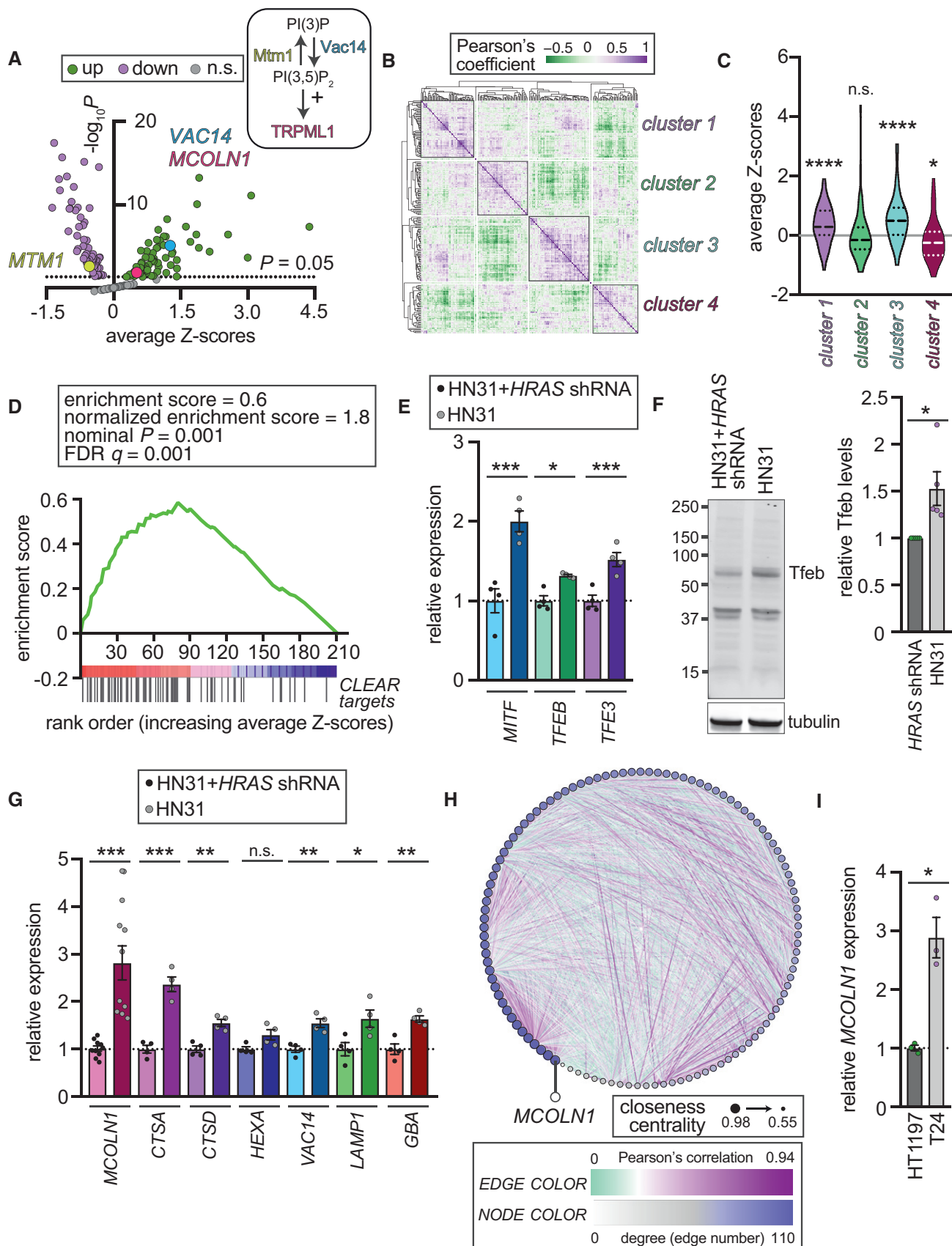


Figure 1.

expression of these endolysosomal genes (Fig EV1A). These data demonstrate *HRAS*-dependent upregulation endolysosomal genes belonging to the CLEAR network.

Biological networks are comprised of sparsely distributed hubs that exhibit disproportionately higher connectivity than other nodes [27]. This architecture bestows robustness to networks since stochastic failures naturally exhibit higher probabilities of impacting the numerous outlying nodes rather than the relatively few hubs. However, focused attacks on hubs can dismantle wide swaths of the network. Based on this understanding, we reasoned that targeting hubs of the endolysosomal gene expression network might impact the growth of oncogenic *HRAS*-induced tumors. To test this idea, we first constructed a network based on pairwise correlations of endolysosomal gene expression in tumors bearing oncogenic *HRAS* mutations. Measures of network centrality revealed that genes belonging to the CLEAR network had higher overall centrality in the network (Fig EV1B). Gene set enrichment analysis performed on the endolysosomal gene set ranked on the basis of centrality scores also pointed to enrichment of CLEAR targets in the centrally placed genes of the network (Fig EV1C). *MCOLN1* had the highest centrality score in the network and a concordantly high number of connections to other genes of the network (Fig 1H). These data suggest that *MCOLN1* is a central node (i.e., a hub) in the network of upregulated endolysosomal genes in *HRAS*-driven cancers.

Is the expression of *MCOLN1* dependent on the presence of oncogenic *HRAS*? To answer this question, we assessed *MCOLN1* expression in T24 cells, which is a urinary tract cancer cell line with naturally occurring *HRAS*^{G12V} mutation [28]. In comparison with a bladder cancer cell line that is wild type for *HRAS* (HT1197 [29]), T24 cells exhibited ~3× increase in *MCOLN1* expression (Fig 1I). Therefore, *MCOLN1* expression in cancer cells is strongly correlated with the presence of oncogenic *HRAS*.

Cancer cells with oncogenic *HRAS* demonstrate elevated TRPML1 activity

To examine whether the increase in *MCOLN1* expression has a functional consequence on TRPML1 channel activity, we performed Ca^{2+} imaging using fura-2 loaded HN31 cells. We evoked endolysosomal Ca^{2+} release by the sequential addition of the TRPML1 agonist, ML-SA1 [30], and the endolysosomolytic agent, glycyl-L-phenylalanine-2-naphthylamide (GPN) [31] in the absence of bath

Ca^{2+} to ensure that entry from the extracellular medium did not contribute to the observed Ca^{2+} transients (Fig 2A and B). In comparison with cells stably expressing *HRAS* shRNA, peak amplitudes of ML-SA1-induced cytosolic Ca^{2+} transients were significantly larger in HN31 cells (Fig 2A–C and E). In contrast, peak amplitudes of GPN-induced transients—evoked after the TRPML1 transients had subsided—were significantly smaller in HN31 cells (Figs 2A, B, D and F). Consequently, ratios of amplitudes of the transients evoked by ML-SA1 and GPN were significantly higher in HN31 compared to cells stably expressing *HRAS* shRNA (Fig 2G). The increase in TRPML1-mediated endolysosomal Ca^{2+} release in HN31 cells was not a function of elevated endolysosomal Ca^{2+} content since the sums of the amplitudes of ML-SA1 and GPN transients—representative of the total endolysosomal $[\text{Ca}^{2+}]$ —were not significantly different in HN31 and the *HRAS* shRNA-expressing variants (Fig 2H). Together, these data indicate that *HRAS*-dependent increase in *MCOLN1* expression results in a proportional elevation of functional TRPML1 channels in HN31 cells (Fig 2I).

TRPML1 is required for the proliferation of cancer cells expressing oncogenic *HRAS*

Treatment of HN31 cells with siRNAs against *MITF* or *TFEB* led to significantly diminished cell proliferation (Fig EV2A) indicating a requirement for the two transcription factors in tumorigenesis. To examine the role of *MCOLN1* expression, we generated HN31 cells that stably express a control shRNA or two independent shRNAs that decreased *MCOLN1* expression (Fig EV2B). Compared to untreated cells or cells that expressed control shRNA, cells that expressed *MCOLN1* shRNAs exhibited diminished proliferation (Fig 3A). Furthermore, *MCOLN1* siRNA, which decreased the expression of the gene in HN31, T24, and HT1197 (Figs EV2B and C), diminished the proliferation of HN31 and T24 cells but not HT1197 cells (Fig 3A). The finding that proliferation of HT1197, which are wild type for *HRAS*, was insensitive to *MCOLN1* knockdown is consistent with the notion that only the cancer cells with oncogenic *HRAS* are vulnerable to *MCOLN1* knockdown. *Vac14* functions with the enzyme PIKfyve to synthesize $\text{PI}(3,5)\text{P}_2$ and, thereby, regulates TRPML1 activation [21,22]. Knockdown of *VAC14* using two independent shRNA constructs, which led to the expected decrease in *VAC14* mRNA (Fig EV2D), decreased the proliferation of HN31 cells (Fig 3B).

Figure 2. TRPML1-mediated endolysosomal Ca^{2+} release in cancer cells with oncogenic *HRAS*.

- A, B Graphs showing the changes in the fura-2 ratio in cells of the indicated genotypes in response to ML-SA1 and GPN. Arrows serve as event markers that denote the points of time at which the drugs were added. Gray lines on top represent the time at which the bath Ca^{2+} was removed. All values represent mean \pm SEM from 3 biological replicates.
- C Same as the data shown in (A) except that the baseline ratios for both genotypes were adjusted to 0 at the start of the experiment. Lines on the right indicate peak amplitudes of Ca^{2+} release in response to the application of ML-SA1. All values represent mean \pm SEM from three biological replicates.
- D Same as (C) except that Ca^{2+} release was evoked using GPN.
- E, F Peak amplitudes of Ca^{2+} release in cells of the indicated genotypes in response to ML-SA1 (E) and GPN (F). All values represent mean \pm SEM. Data points represent values from biological replicates. Statistical test employed was Student's *t*-test.
- G Ratio of the amplitudes of Ca^{2+} release in cells of the indicated genotypes in response to ML-SA1 and GPN. All values represent mean \pm SEM. Data points represent values from biological replicates. Statistical test employed was Student's *t*-test.
- H Total Ca^{2+} release in cells of the indicated genotypes in response to ML-SA1 and GPN. All values represent mean \pm SEM. Data points represent values from biological replicates. Statistical test employed was Student's *t*-test.
- I Schematic representation of the notion that an increase in the expression of *MCOLN1* results in a proportional increase in ML-SA1-induced Ca^{2+} release in HN31 cells.

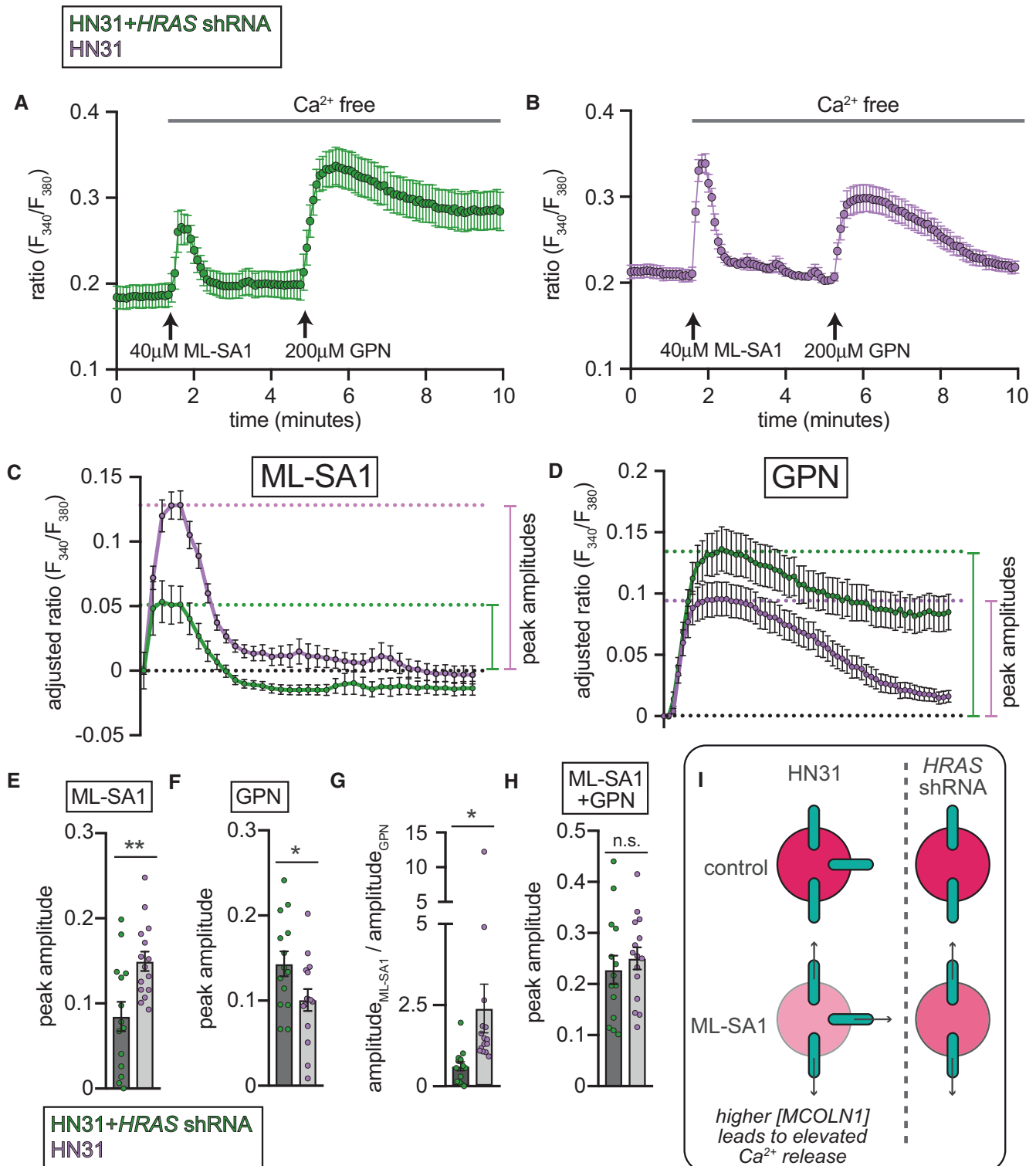


Figure 2.

Application of a pharmacological inhibitor of TRPML1 (ML-SI1) [32] also significantly diminished proliferation of the *HRAS*^{G12V} transformed oral cancer cells, UM-SCC-22A-*HRAS*^{G12V} (Figs 3C and EV2E) [33]. In contrast, proliferation of UM-SCC-22A-*HRAS*^{WT} cells, which express wild-type *HRAS*, was not affected by ML-SI1

application (Figs 3C and EV2E). Furthermore, application of ML-SI1 significantly attenuated the proliferation of HN31 and T24 cells but not HT1197 or the cells that stably express *HRAS* shRNA (Figs 3C and EV2E and F). The PIKfyve inhibitor, YM201636, which inhibits PI(3,5)P₂ synthesis and TRPML1 activation [34,35], also diminished

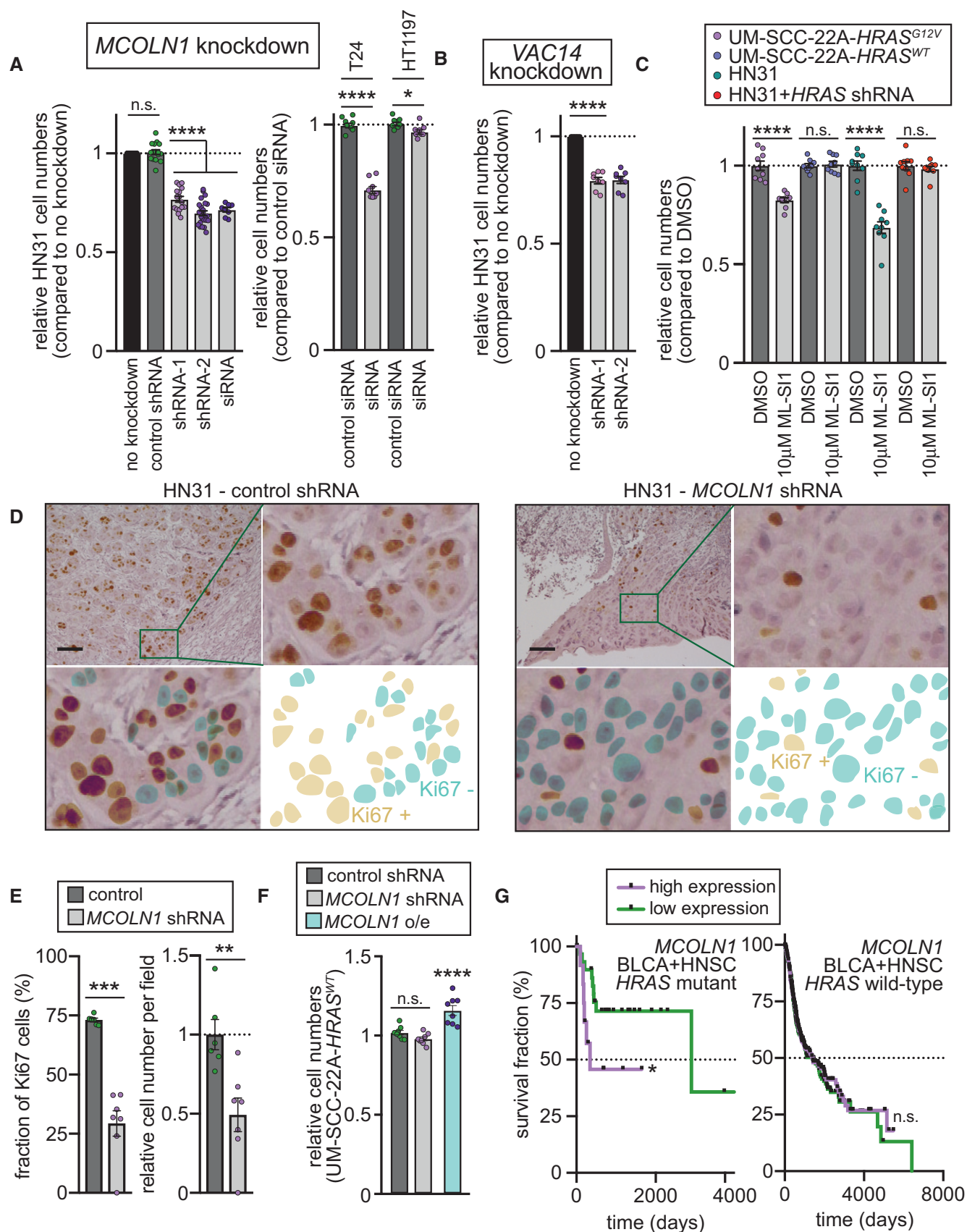


Figure 3.

Figure 3. *MCOLN1* expression is necessary and sufficient for proliferation of cells expressing oncogenic *HRAS*.

- A–C Bar graphs showing the relative cell numbers in the indicated cell types following the indicated treatments. Cell numbers were assessed after a 48-h period of growth in cultures seeded at equal densities. All values represent mean \pm SEM. Data points represent values from biological replicates. Statistical test employed was pairwise Student's *t*-tests with Bonferroni *post hoc* correction to account for multiple pairwise testing in (A) and (B).
- D Representative images showing Ki67-labeling in xenografts generated from implantation of HN31 cells stably expressing control shRNA (left) or *MCOLN1* shRNA (right). Pseudocolored panels show the representative distribution Ki67 positive or negative nuclei. Scale bars shown (0.5 mm) apply to all panels.
- E Bar graphs showing fraction (left) and total number (right) of Ki67 labeled nuclei in the indicated cell types. All values represent mean \pm SEM. Values in the bar graph on the right were normalized to control mean. Data points represent values from independent eggs. Statistical test employed was Student's *t*-test.
- F Bar graphs showing the relative cell numbers in UM-SCC-22A-*HRAS*^{WT} cells following the indicated perturbations. All values represent mean \pm SEM. Data points represent values from biological replicates. Statistical test employed was Student's *t*-test.
- G Kaplan–Meier curves showing the survival of patients stratified on the basis of *MCOLN1* expression in BLCA and HNSC patients whose tumors were wild type for *HRAS* (right) or carried oncogenic *HRAS* mutations (left). Statistical test employed was the Mantel–Cox log-rank test.

the proliferation of UM-SCC-22A-*HRAS*^{G12V} and HN31 cells (Fig EV2G). However, proliferation of cells that do not express oncogenic *HRAS* was not affected by YM201636 (Fig EV2G). These data indicate that proliferation of cancer cells expressing oncogenic, but not wild-type, *HRAS* is vulnerable to TRPML1 inhibition.

Next, we performed the chick chorioallantoic membrane (CAM) assay as an *in vivo* xenograft model [36,37] to examine the effects of *MCOLN1* knockdown and ML-SI1 application on the ability of HN31 cells to form tumors. CAM xenografts generated by growing human cancer cells histologically resemble tumors grown in mouse xenograft models [36,37]. These cost-effective, fast, and reproducible xenografts can be used to examine cancer cell proliferation using Ki67-labeling as an indicator and the influence of various drugs thereupon. In xenografts grown with HN31 cells expressing control shRNA, ~75% cancer cell nuclei were Ki67-positive (Fig 3D and E). In contrast, only ~30% of nuclei were Ki67-positive in xenografts grown with HN31 cells stably expressing an shRNA against *MCOLN1* (Fig 3D and E). *MCOLN1* knockdown also reduced the total number of cancer cells per field (Figs 3D and E). Similarly, application of ML-SI1 significantly decreased the fraction of Ki67-labeled nuclei (Appendix Fig S2A). However, the total number of HN31 cells per field was not significantly diminished in eggs treated with ML-SI1 (Appendix Fig S2B). Since ML-SI1 was added 1 and 3 days after the initial implantation of xenografts, our data suggest that subsequent attenuation of cell proliferation was not sufficient to significantly decrease cell numbers. On the other hand, implantation of HN31 stably expressing *MCOLN1* shRNA likely proliferated slowly from the beginning, allowing for significant decreases in both Ki67-labeled cells and total cell number.

Expression of *HRAS*^{G12V}, but not *HRAS*^{WT}, was sufficient to potentiate *MCOLN1* expression in UM-SCC-22A cells (Appendix Fig S2C). Furthermore, knockdown of *MCOLN1* did not alter the proliferation of UM-SCC-22A-*HRAS*^{WT} cells (Fig 3F). These data demonstrated reliable correlation between *MCOLN1* expression and *HRAS*^{G12V}-driven cancer cell proliferation. Notably, ectopic overexpression of *MCOLN1* in UM-SCC-22A-*HRAS*^{WT} was sufficient to enhance the rate of cell proliferation (Fig 3F) indicating that *MCOLN1* expression is necessary and sufficient for potentiation of cancer cell proliferation.

***MCOLN1* expression correlates with prognosis of BLCA and HNSC patients**

We asked whether the prognosis of cancer patients with tumors carrying activating mutations in *HRAS* correlated with *MCOLN1* expression. In cases of BLCA and HNSC, stratifying patients with oncogenic *HRAS* mutations into high and low *MCOLN1* expressors revealed that lower

MCOLN1 expression correlated with significantly improved patient survival (Fig 3G). In patients that were wild type for *HRAS*, however, we found no correlation between *MCOLN1* expression and patient prognosis (Fig 3G). Consistent with the idea that *MTM1* encodes a lipid phosphatase that indirectly diminishes TRPML1 activity, higher expression of *MTM1* correlated with improved patient survival (Appendix Fig S2D). Once again, in patients that were wild type for *HRAS*, we observed no correlation between *MTM1* expression and patient prognosis (Appendix Fig S2D). Thus, patterns of gene expression predicted to favor elevated TRPML1 activity tracked with poorer survival of BLCA and HNSC patients with oncogenic *HRAS* mutations. The prognosis of THCA patients was generally very good with very few fatalities being associated with this disease (Appendix Fig S2E). Accordingly, *MCOLN1* expression was not related to survival in THCA patients either with or without *HRAS* mutations (Appendix Fig S2E).

TRPML2 and TRPML3 exhibit partial roles in the proliferation of cancer cells with oncogenic *HRAS*

TRPML2 and TRPML3 (encoded by *MCOLN2* and *MCOLN3*, respectively) are TRPML1 paralogs, which heteromultimerize with TRPML1 and potentially influence its function [38]. Since ML-SI1 partially inhibits the TRPML1 paralogs [32], we assessed the contributions of TRPML2 and TRPML3 to *HRAS*-driven cancer cell proliferation. Neither *MCOLN2* nor *MCOLN3* were significantly altered in BLCA, THCA, and HNSC with mutant *HRAS* (Fig EV3A), although both genes were modestly upregulated in HN31 cells (Fig EV3B). Consistent with the changes in gene expression, knockdown of either *MCOLN2* or *MCOLN3* in HN31 cells led to slight (~10%) decreases in cell proliferation (Fig EV3C and D). Simultaneous knockdown of both *MCOLN1* and *MCOLN2*, but not *MCOLN1* and *MCOLN3*, additively attenuated HN31 cell proliferation, i.e., *MCOLN2* shRNA decreased the proliferation of cells with *MCOLN1* knockdown by an additional ~10% (Fig EV3D). These data suggest non-redundant roles for TRPML1 and TRPML2 in cancer cell proliferation. Application of ML-SI1 after *MCOLN1* knockdown decreased cell proliferation to the same extent as that induced by *MCOLN2* shRNA (~10%), which is consistent with the “pan TRPML” effects of the drug [32].

TRPML1 inhibition attenuated ERK phosphorylation in cells expressing oncogenic *HRAS*

HRAS is a “molecular switch” that toggles between GTP or GDP-bound states [39]. In the GTP bound state, *HRAS* potentiates mitogenic pathways including the RAF–MEK–ERK kinase cascade.

Oncogenic mutations promote the active HRAS configuration and, thereby, evoke unrestricted ERK phosphorylation and cell proliferation. Indeed, stable overexpression of GFP-tagged HRAS^{G12V} in Madin-Darby Canine Kidney (MDCK) cells was sufficient to increase ERK phosphorylation (Fig 4A and B). ERK phosphorylation in HN31 cells was also dependent on oncogenic HRAS as evidenced by our finding that knockdown of HRAS decreased the pERK/ERK ratio (Fig 4C and E). Application of ML-SI1 significantly reduced the pERK/ERK ratio, but only in those cells that expressed HRAS^{G12V} (Fig 4A and B). The pERK/ERK ratio was not changed in control MDCK cells in response to ML-SI1. These effects of ML-SI1 were not due to alterations in the expression levels of GFP-HRAS^{G12V} (Appendix Fig S3A–C). Knockdown of MCOLN1 in HN31 cells, but not cells stably expressing HRAS shRNA, also decreased ERK phosphorylation (Fig 4C and E, and Appendix Fig S3D and E). In T24 cells, either MCOLN1 knockdown or application of ML-SI1 decreased ERK phosphorylation, whereas neither MCOLN1 knockdown nor ML-SI1 influenced the pERK/ERK ratio in HT1197 cells, which are wild type for HRAS (Fig 4D and F). Taken together, these data demonstrate that pharmacological inhibition of TRPML1 or MCOLN1 knockdown attenuated ERK phosphorylation in only those cells that express oncogenic variants of HRAS.

Effects of oncogenic RAS on cell proliferation and ERK phosphorylation is diminished in *Drosophila* lacking the MCOLN1 ortholog

To further assess the relationship between RAS–ERK signaling and TRPML1 expression, we utilized *Drosophila* lacking the sole MCOLN1 ortholog, *trpml* [40], as a genetically tractable model. Loss of fly *trpml* leads to phenotypes that are remarkably similar to those observed in human cells lacking MCOLN1 [40]. Importantly, expression of human MCOLN1 suppressed mutant phenotypes when expressed in *trpml* null flies (*trpml*¹) [41]. We found that ectopic expression of the activated variant of the fly RAS homolog (*dRas*^{G12V}) [42] in glia led to a significant increase in *trpml* expression (Fig 5A). Coexpression with GFP allowed us to detect *dRas*^{G12V}-induced proliferation of glial cells in the larval brain (Fig 5B). Expression of *dRas*^{G12V} and GFP in *trpml*¹ glia led to a significantly attenuated phenotype (Figs 5B and C). Quantification of the relative volume of GFP-expressing cells in the larval brain indicated a ~25% decrease in glial volume in *trpml*¹ expressing *dRas*^{G12V} (Fig 5C).

Next, we asked whether *dRas*^{G12V}-induced ERK phosphorylation is dependent on TRPML. Because the fraction of glial cells in the larval brain is low (~10% of the cell in the larval brain are glia), we

examined ERK phosphorylation in larval macrophages and fat bodies, which constitute abundant sources of readily accessible cells. Expression of *dRas*^{G12V} in larval macrophages led to increased levels of tubulin, total ERK, and ERK phosphorylation (Fig 5D and E and Appendix Fig S4), which is consistent with an increase in cell proliferation. The pERK/tubulin ratio (~8× higher in *dRas*^{G12V}-expressing macrophages) and pERK/ERK ratio were significantly attenuated in cells lacking *trpml* (Fig 5D and E, and Appendix Fig S4). The pERK/tubulin and pERK/ERK ratios were statistically indistinguishable in wild-type and *trpml*¹ macrophages not expressing *dRas*^{G12V} (Fig 5D and E, and Appendix Fig S4).

Since flies do not express an HRAS-equivalent gene, we ectopically expressed human HRAS^{G12V} in *Drosophila* larval fat bodies—an endocrine organ with features similar to human adipocytes and liver. HRAS^{G12V} led to ~8× increase in ERK phosphorylation (Fig 5F and G). These data demonstrate that activated human HRAS is able to couple with the appropriate signaling cascade in fly tissues and elicit ERK phosphorylation. As with *dRas*^{G12V}, expression of human HRAS^{G12V} in *trpml*¹ tissues led to dramatically diminished ERK phosphorylation (Fig 5F and G). Taken together, the data in flies agree with our findings in human cancer cells and demonstrate an evolutionarily conserved requirement for TRPML1 in RAS-induced ERK phosphorylation and cell proliferation.

Inhibition of TRPML1 diminished clustering and localization of HRAS^{G12V} at the plasma membrane

Activation of the RAF–MEK–ERK cascade depends on formation of RAS nanoclusters at the plasma membrane [43,44]. Accordingly, disruption of the clustering of oncogenic HRAS severely restricts downstream ERK phosphorylation and, consequently, limits cell proliferation. Given the effects of TRPML1 inhibition of ERK phosphorylation and cell proliferation, we used quantitative super-resolution electron microscopy (EM) spatial analysis to examine HRAS^{G12V} nanoclusters at the plasma membrane in response to ML-SI1. We prepared intact basolateral plasma membrane sheets from GFP-HRAS^{G12V} expressing cells that were attached on EM grids with gold-conjugated anti-GFP antibodies (Fig 6A). Using transmission EM at 100,000× magnification, we imaged gold labeling on the intact plasma membrane sheets. Subsequently, we calculated the spatial distribution of the gold-labeled GFP-HRAS^{G12V} within a 1 μm² area using the Ripley's univariate K-function analysis as described [43]. The summary of the clustering data, L_{max}, indicated a reduction in the extent of HRAS^{G12V} nanoclustering in ML-SI1-treated cells (Fig 6B). Furthermore, the number of gold particles within the

Figure 4. TRPML1 inhibition or MCOLN1 knockdown attenuated ERK phosphorylation in mammalian cells expressing activated HRAS.

- A Representative Western blots generated using extracts from cells of expressing oncogenic HRAS and controls treated with ML-SI1 as indicated. The primary antibodies used are indicated on the right.
- B Bar graph showing quantification of the Western blots shown in (A). All values represent mean ± SEM. Data points represent values from biological replicates. Statistical test employed was Student's *t*-test.
- C, D Representative Western blots generated using extracts from the indicated cell types after the indicated perturbations. Primary antibodies used are indicated on the right.
- E Bar graph showing quantification of the Western blots in (C). All values represent mean ± SEM. Data points represent values from biological replicates. Statistical test employed was Student's *t*-test.
- F Bar graph showing quantification of the Western blots in (D). All values represent mean ± SEM. Data points represent values from biological replicates. Statistical tests employed were Student's *t*-test and ANOVA.

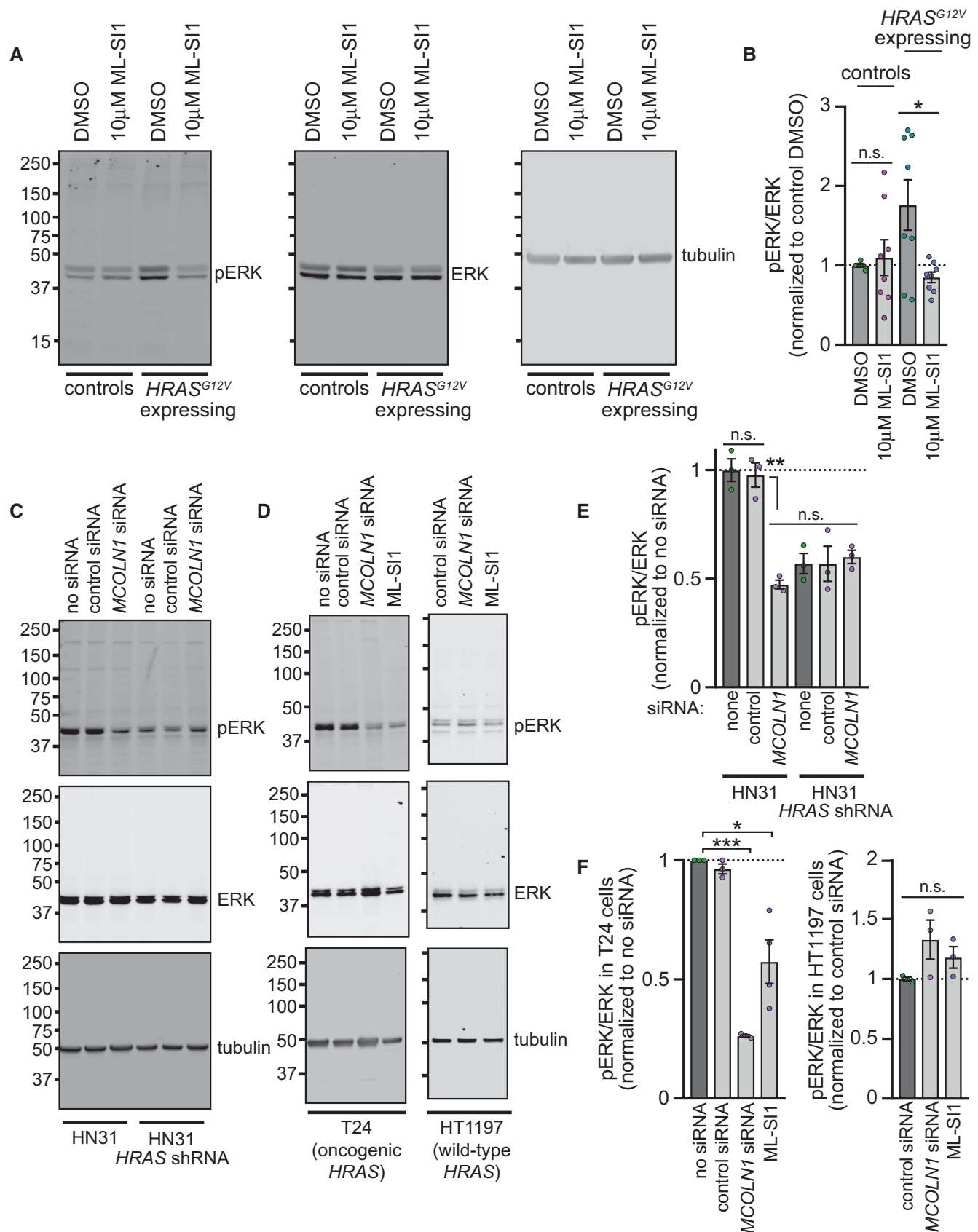


Figure 4.

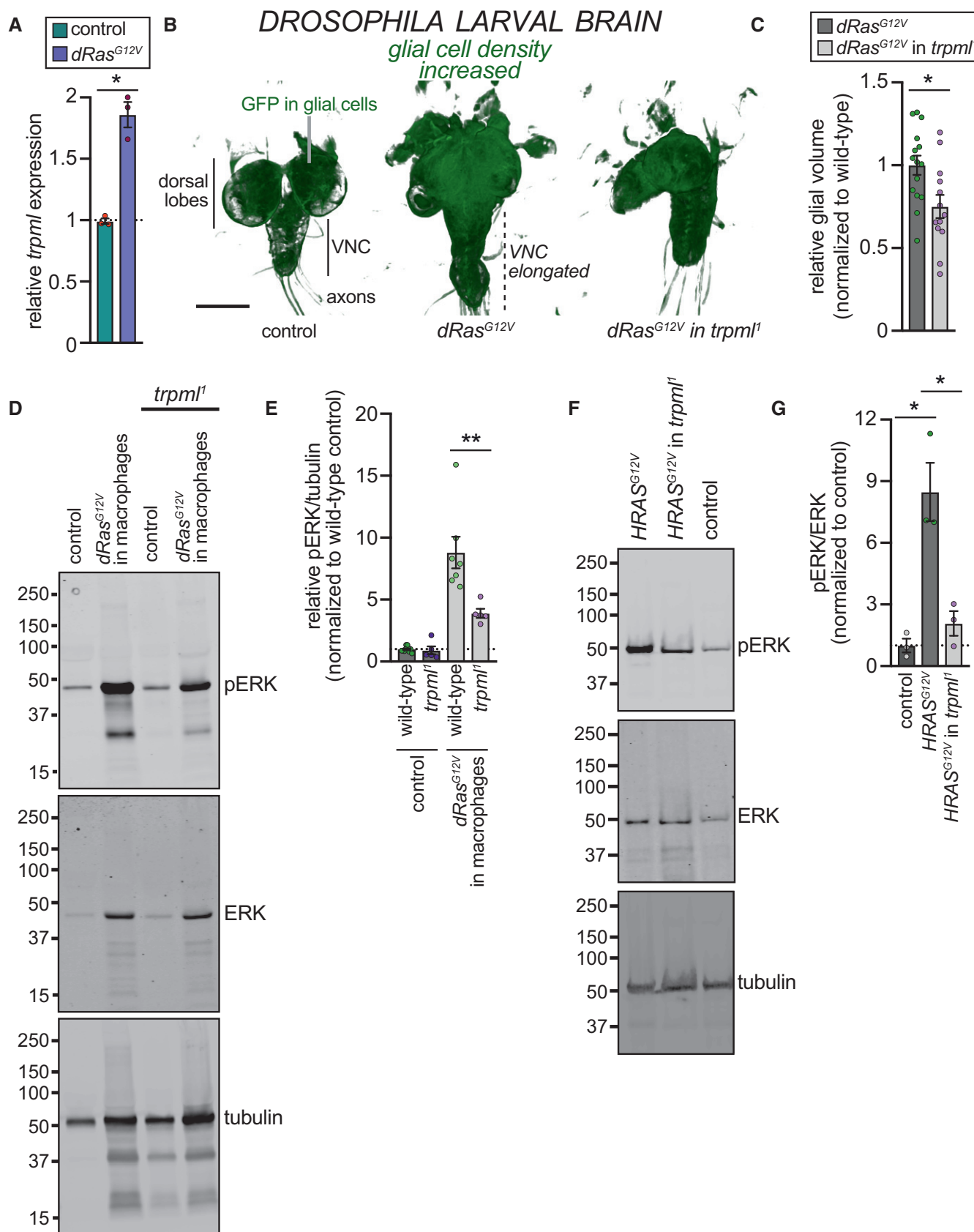


Figure 5.

Figure 5. Effects of oncogenic *dRas* on cell proliferation and ERK phosphorylation are attenuated in *trpml*-deficient *Drosophila*.

- A Bar graph showing relative levels of *trpml* mRNA in *Drosophila* larval brain extracts from control animals and animals expressing *dRas*^{G12V} in glia. All values represent mean \pm SEM. Data points represent values from biological replicates. Statistical test employed was Student's *t*-test.
- B Representative images of *Drosophila* 3rd-instar larvae expressing the indicated transgenes in glial cells. *repo-GAL4* was used to drive the expression of *UAS-dRas*^{G12V} in glia. Images shown are volumetric reconstructions of confocal stacks. The various anatomical structures of the larval brain are annotated. VNC refers to the "ventral nerve chord", which is distinct from dorsal hemispheres of the brain. GFP staining represents the total glial membranes in the larval brains. Scale bar, 100 μ m.
- C Bar graph showing relative glial cell volume in larvae of the indicated genotypes. All values represent mean \pm SEM. Data points represent values from biological replicates. Statistical test employed was Student's *t*-test.
- D Representative Western blots generated using macrophage extracts isolated from 3rd-instar larvae of the indicated genotypes. *He-GAL4* was used to drive the expression of *UAS-dRas*^{G12V} in macrophages. The primary antibodies used are indicated on the right.
- E Bar graph showing quantification of the Western blots shown in (D). All values represent mean \pm SEM. Data points represent values from biological replicates. Statistical test employed was Student's *t*-test.
- F Representative Western blots generated using fat-body extracts isolated from 3rd-instar larvae of the indicated genotypes. *cg-GAL4* was used to drive the expression of *UAS-HRAS*^{G12V} in larval fat bodies. The primary antibodies used are indicated on the right.
- G Bar graph showing quantification of the Western blots shown in (F). All values represent mean \pm SEM. Data points represent values from biological replicates. Statistical test employed was Student's *t*-test.

1 μ m² area—an estimate of the level of GFP-HRAS^{G12V} on the cell surface—was significantly reduced in ML-SI1-treated cells (Fig 6C).

Lateral segregation of GTP- and GDP-bound HRAS depends on the levels of plasma membrane cholesterol [45,46]. Interestingly, nanoclustering of HRAS^{G12V} was significantly restored in ML-SI1-treated cells upon addition of exogenous cholesterol (Fig 6B). In contrast, addition of phosphatidylserine (PS), a major lipid constituent of the inner leaflet of the plasma membrane that is required for KRAS^{G12V} clustering [47], did not restore the clustering of HRAS^{G12V} (Fig 6B). Addition of exogenous cholesterol also restored the plasma membrane localization of HRAS^{G12V} as evidenced by the number of gold particles in the plasma membrane sheets (Fig 6C). Knockdown of *MCOLN1* also decreased both the clustering and plasma membrane levels of GFP-HRAS^{G12V} (Figs 6D and E, and EV4A). Furthermore, exogenously added cholesterol was sufficient to elevate the clustering of GFP-HRAS^{G12V} in control cells and prevented *MCOLN1* knockdown from attenuating GFP-HRAS^{G12V} clustering (Fig 6D). Application of a statin (20 μ M Simvastatin) also diminished GFP-HRAS^{G12V} clustering and levels at the plasma membrane (Fig 6D and E), which demonstrates necessity for cholesterol in HRAS^{G12V} clustering. Lastly, exogenous application of cholesterol for 3 h was sufficient to ablate the differences in ERK phosphorylation observed in HN31 cells that express *MCOLN1* shRNA (Fig 6F and G). The cholesterol-induced increase in ERK phosphorylation in control HN31 cells (Fig 6F and G) likely reflects the increase in HRAS^{G12V} clustering evoked by exogenous cholesterol (Fig 6D).

ML-SI1 and statin also decreased the nanoclustering of GFP-HRAS^{WT} (Fig EV4B). Diminished GFP-HRAS^{WT} clustering in ML-SI1-treated cells was fully restored by exogenous cholesterol (Fig EV4B). Intriguingly, neither ML-SI1 nor statin influenced the levels of GFP-HRAS^{WT} in the inner leaflet of the plasma membrane (Fig EV4C). These data indicate that both the nanoclustering and optimal plasma membrane localization of HRAS^{G12V} depend on TRPML1 (Fig 6H), whereas only the clustering of wild-type HRAS was sensitive to lowered TRPML1 function (Fig 6H). Given that both plasma membrane localization and nanoclustering affect the signal output of HRAS [48–50], the distinct effects of TRPML1 inhibition on HRAS^{G12V} compared to HRAS^{WT} explain the selective vulnerability of oncogenic HRAS-expressing cancer cells to TRPML1 inhibition.

To validate the necessity for cholesterol in HRAS^{G12V}-dependent cell proliferation, we assessed the effects of cholesterol depletion on

HN31 cell proliferation. Consistent with critical roles for membrane cholesterol in myriad cellular signaling events, proliferation of both control HN31 cells and HN31 cells expressing HRAS shRNA was diminished by β -cyclodextrin albeit with differing sensitivities (Fig EV5A). Analyses of the dose sensitivities of β -cyclodextrin-induced decrease in cell proliferation revealed that HN31 cells expressing HRAS shRNA exhibited significantly higher repression coefficient (*K_i*) values than control HN31 cells (Fig EV5B). Similarly, proliferation of HN31 cells and the variants stably expressing HRAS shRNA were diminished when the cells were grown in the presence of different doses of statin (Fig EV5C), with HN31 cells expressing HRAS shRNA $\sim 2\times$ higher *K_i* values (Fig EV5D). These data indicate that cancer cells with oncogenic HRAS exhibited greater sensitivity to cholesterol depletion and thus point to a necessary role for cholesterol in the proliferation of those cells.

TRPML1 is required for processing and trafficking of cholesterol in endolysosomes

Cholesterol trafficking is intimately coupled to endolysosomal function. Lysosomal proteins such as NPC1 and NPC2 have well-established roles in cholesterol extrusion from endolysosomes [51]. Since TRPML1 is required for the exocytosis of endosomal vesicles (Fig 7A) [32,52,53], it stands to reason that TRPML1 mediates the recycling of endolysosomal cholesterol back to the plasma membrane (Fig 7A). Additionally, TRPML channels are required for the fusion of late endosomes with lysosomes [54], which is necessary for de-esterification of endocytosed cholesterol esters (Fig 7A). Thus, we hypothesized that inhibition of TRPML1 would result in diminished plasma membrane cholesterol levels stemming from aberrant intracellular accumulation of cholesterol and inadequate de-esterification of cholesterol esters.

Although neither ML-SI1 nor shRNA-mediated *MCOLN1* knockdown affected the levels of total cholesterol in HN31 cells (comprised of both free and esterified cholesterol) (Fig 7B), the fraction of free cholesterol was significantly decreased in response to either perturbation (Fig 7C). A decrease in free cholesterol without significant changes in total cholesterol is consistent with diminished de-esterification. Similarly, the fraction of free cholesterol was $\sim 25\%$ lower in *Drosophila* brain tissues lacking *trpml* (Fig 7D). Thus, TRPML proteins have an evolutionarily conserved role in cholesterol de-esterification and maintenance of free cholesterol levels.

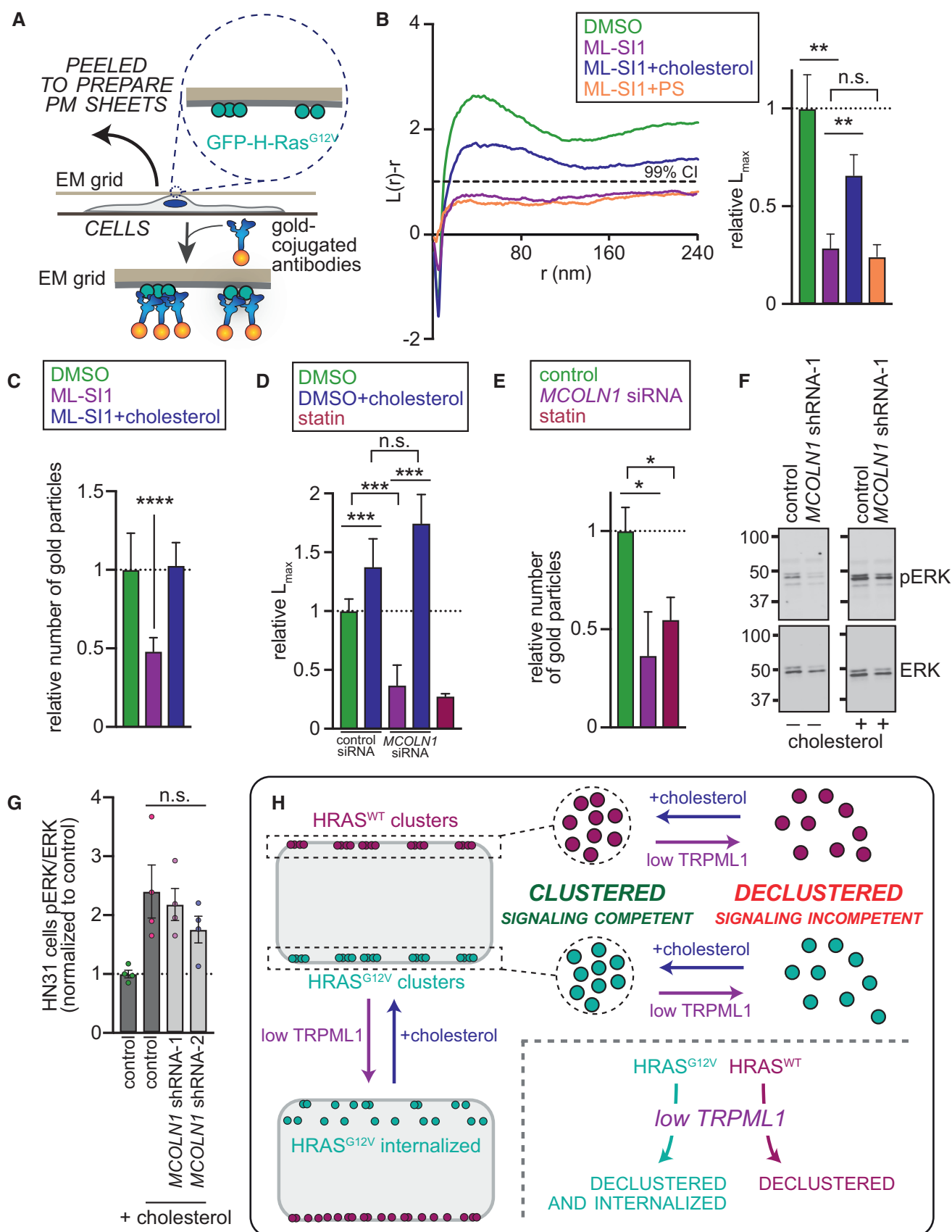


Figure 6.

Figure 6. TRPML1 is required for nanoclustering and levels of HRAS^{G12V} at the plasma membrane.

- A Schematic showing the methodology utilized for preparation of plasma membrane sheets from MDCK cells expressing GFP-HRAS^{WT} or GFP-HRAS^{G12V}. After preparation of plasma membrane sheets, gold-conjugated antibodies are used to visualize clusters of GFP-tagged proteins in electron micrographs.
- B Weighted mean univariate K-function curves of immunogold labeled GFP-HRAS^{G12V} under indicated conditions, $n \geq 15$ for each condition. The gold point patterns were analyzed with univariate K-functions expressed as $L(r)$ - r . The bar graph on the right shows the peak value L_{max} of the $L(r)$ - r curve, which represents the extent of GFP-HRAS^{G12V} nanoclustering. Values are normalized to DMSO average and represent mean \pm SEM ($n \geq 15$ for each condition). Statistical significances of differences were evaluated in bootstrap tests.
- C Bar graph showing GFP-HRAS^{G12V} content in the inner leaflet of the plasma membrane is quantified as the number of gold particles per $1 \mu\text{m}^2$ region from electron micrographs. Values are normalized to DMSO average and represent mean \pm SEM, $n \geq 15$ for each condition. Statistical test employed was Student's *t*-test with Bonferroni *post hoc* correction to account for multiple pairwise comparisons.
- D The extent of GFP-HRAS^{G12V} nanoclustering quantified by L_{max} values in cells exposed to the indicated perturbations. Values are normalized to DMSO average and represent mean \pm SEM ($n \geq 15$ for each condition). Statistical significances of differences were evaluated in bootstrap tests.
- E Same as (C) but in cells exposed to the indicated perturbations. Values shown are normalized to DMSO average.
- F Representative Western blots generated using extracts from HN31 cells stably expressing the *MCOLN1* shRNA. Samples treated with exogenous cholesterol for 3 h are indicated at the bottom. Primary antibodies used are indicated on the right.
- G Bar graph showing quantification of the Western blots in (F). All values represent mean \pm SEM. Data points represent values from biological replicates. Statistical test employed was ANOVA.
- H Schematic summarizing the effects of decreased TRPML1 activity on HRAS^{WT} and HRAS^{G12V}. Our data indicate that TRPML1 inhibition diminished HRAS^{G12V} nanoclustering and plasma membrane levels. Addition of cholesterol restored these parameters. Only the nanoclustering of HRAS^{WT} was affected by ML-SI1.

To assess subcellular distribution of cholesterol, we examined the localization of a fluorescently tagged sensor of cholesterol, mCherry-D4H [55]. As described previously [8], confocal imaging of MDCK cells revealed that the majority of mCherry-D4H decorated the plasma membrane of the cells (Fig 7E). However, within 24 h of ML-SI1 application, most of the mCherry-D4H signal relocated to intracellular vesicles leading to a significant increase in the number of intracellular mCherry-D4H puncta (Figs 7E and F). We found that the mCherry-D4H puncta colocalized with endolysosomal membrane protein, LAMP1-GFP (Fig 7G), which indicates that TRPML1 inhibition caused the cholesterol sensor to be trapped in endolysosomes. In HN31 cells, we evaluated the distribution of cholesterol using the cholesterol-binding polyene antibiotic, filipin [56], as a fluorescent. We found that *MCOLN1* knockdown led to redistribution of filipin from the plasma membrane to intracellular punctae (Fig 7H), which we quantified as an increase in the fraction of cellular area stained with filipin (Fig 7I). ML-SI1 treatment also led to the mislocalization of the recombinant sphingomyelin sensor, GFP-lysenin [57], from the plasma membrane to internal vesicles (Fig EV5E). Since sphingomyelin resides in cholesterol-enriched microdomains, these data demonstrate that inhibition of TRPML1 leads to the anomalous accumulation of cholesterol-laden microdomains in endolysosomes. Taken together, these data demonstrate that inhibition of TRPML1 leads to a redistribution of cholesterol.

Concomitant with aberrant endolysosomal localization of mCherry-D4H and GFP-lysenin, ML-SI1 treatment depleted these markers from the plasma membrane (Figs 7E and EV5E). To examine whether biophysical properties of the membrane in ML-SI1-treated cells reflect the depletion of cholesterol from the plasma membrane, we prepared giant plasma membrane vesicles (GPMVs) [58] from control and ML-SI1-treated cells. Lipid constituents of GPMVs closely mimic those of the plasma membrane, and phase separation of raft and non-raft markers in GPMVs reflects the propensity for cholesterol-induced ordered domain formation in mammalian membranes [59]. We found that GPMVs isolated from ML-SI1-treated cells exhibited a decrease in the phase separation temperature (miscibility temperature) in comparison with GPMVs isolated from vehicle-treated cells (Figs 7J and

K). Since miscibility temperature is related to the lifetime of membrane nanodomains and is regulated by cholesterol content [60], our data indicate that TRPML1 inhibition significantly influences the physical properties of the plasma membrane via disruption of cholesterol content of the plasma membrane. Consistent with this deduction, direct cholesterol depletion has a similar effect of reducing the fraction of phase-separated GPMVs [60]. Further supporting a role for cholesterol, we found that exogenous application of cholesterol prevented the decrease in GPMV miscibility temperature in ML-SI1-treated cells, whereas exogenous cholesterol did not influence the miscibility temperature of GPMVs generated from vehicle-treated cells (Fig 7J and K). These data indicate that ML-SI1 treatment results in alteration of plasma membrane physical properties in a manner consistent with diminished cholesterol levels in that compartment.

Discussion

Using a combination of bioinformatic analyses of human tumors and experimental assessment of multiple cancer cell lines, we identified a gene expression signature in *HRAS*-positive tumors that points to involvement of the Mitf/Tfe3/Tfeb transcription factors [14–16,61]. Indeed, expression of *MITF*, *TFEB*, and *TFE3* was elevated in cells with oncogenic *HRAS* mutations. Concordantly, knockdown of either *MITF* or *TFEB* led to a decrease in the proliferation of the HN31 oral cancer cell line. These findings, which suggest partially redundant functions of these transcription factors in cancer cell proliferation, are in agreement with previous reports of Mitf/Tfe3/Tfeb-induced endolysosomal biogenesis in potentiation of tumorigenesis [9,62].

How could we leverage this understanding to develop strategies to mitigate the activation of these transcription factors in cancer? Since drugs that directly block Mitf/Tfe3/Tfeb are not available, indirect approaches via stimulation of mTORC1 or inhibition of calcineurin to arrest nuclear import of these transcription factors [15,26,63] could mitigate unremitting endolysosomal biogenesis. However, cancer-related alterations preemptively decouple the nucleocytoplasmic transport of Mitf/Tfe3/Tfeb from mTORC1 [9], potentially

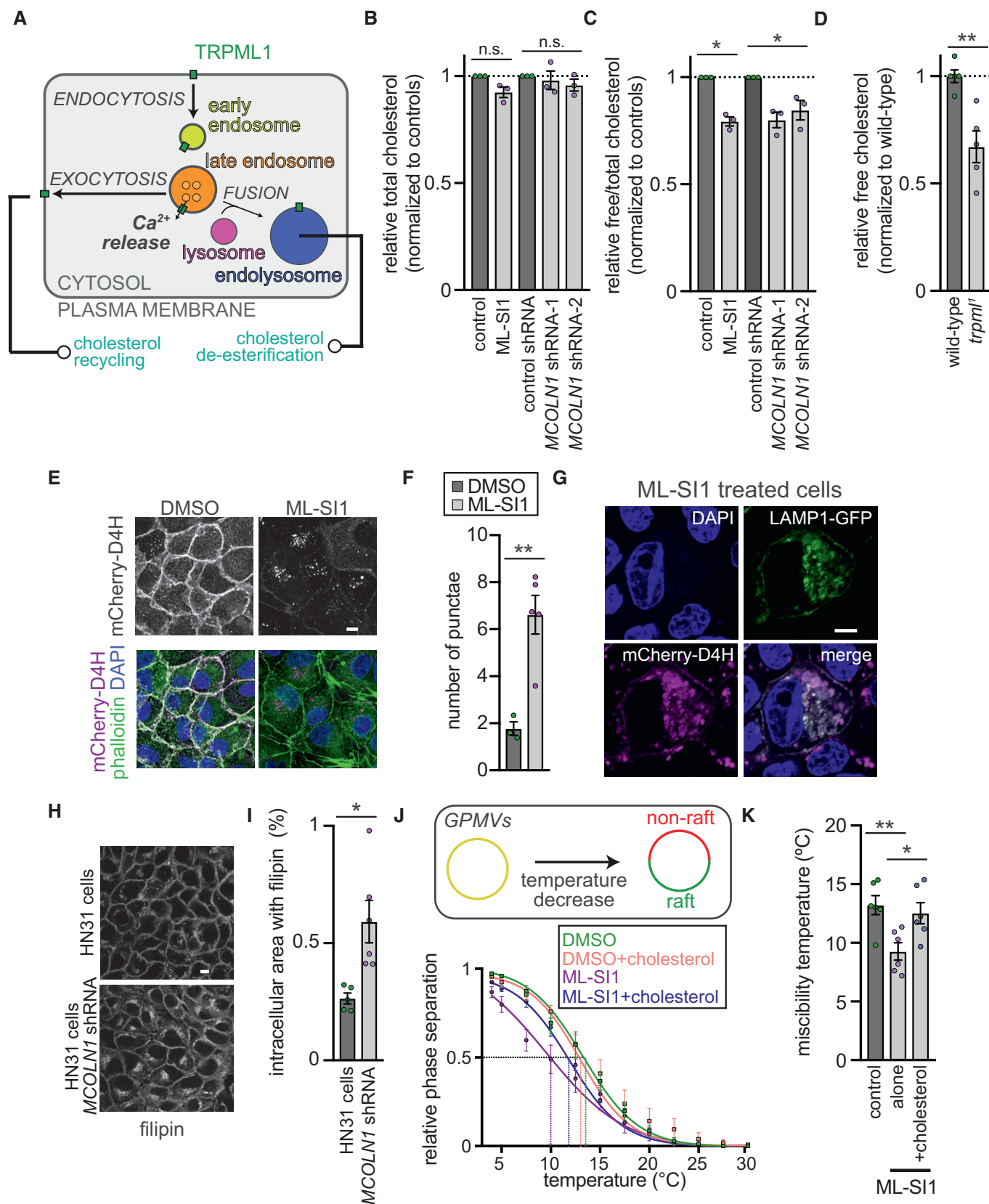


Figure 7.

Figure 7. TRPML1 inhibition results in diminished de-esterification and redistribution of cellular cholesterol.

- A Schematic showing the role of TRPML1 in vesicular trafficking. TRPML1 is active in the membrane of late endosomes and facilitates fusion of these vesicles with lysosomes or the plasma membrane. Channels delivered to the plasma membrane are redelivered to the late endosomes via endocytosis. Whereas delivery of vesicles to the lysosomes is required for cholesterol de-esterification in that compartment, vesicular fusion with the plasma membrane is required for cholesterol recycling.
- B–D Bar graph showing the relative levels of total or free/total cholesterol in HN31 cell extracts exposed to the indicated perturbagens (B–C), or larval brain extracts from animals of the indicated genotypes (D). Values represent mean \pm SEM. Data points represent values from biological replicates. Statistical tests employed were Student's *t*-test and ANOVA.
- E Confocal images of MDCK cells expressing mCherry-D4H. Colocalization with the cortical actin (phalloidin) indicates that mCherry-D4H is predominantly localized to the plasma membrane in DMSO treated cells. Within 24 h of ML-SI1 treatment, the mCherry-D4H redistributes to intracellular punctae. Although minimal mCherry-D4H signal remained at the plasma membrane in ML-SI1-treated cells, the phalloidin signal (cortical actin) remained unchanged. Scale bar (10 μ m) shown in the panel on the top right applies to all panels.
- F Bar graph showing quantification of mCherry-D4H punctae in DMSO or ML-SI1-treated cells. All values represent mean \pm SEM. Data points represent values from biological replicates. Statistical test employed was Student's *t*-test.
- G Confocal images of MDCK cells expressing mCherry-D4H and LAMP1-GFP treated with ML-SI1. Scale bar (10 μ m) shown in the panel on the top right applies to all panels.
- H Confocal images of control and *MCOLN1* shRNA-expressing HN31 cells treated with the cholesterol sensor, filipin. Scale bar (10 μ m) shown in the panel on the top applies to both panels.
- I Bar graph showing the quantification of the internalized filipin staining in HN31 cells after *MCOLN1* knockdown. All values represent mean \pm SEM. Data points represent values from biological replicates. Statistical test employed was Student's *t*-test.
- J Fraction of phase-separated GPMVs at the indicated temperatures. Colors of the lines indicate the treatment conditions of MDCK cells prior to generation of GPMVs. Dashed vertical lines indicate the miscibility temperature of the indicated populations of GPMVs. Values shown represent mean \pm SEM. Lines were generated by fitting the data to sigmoidal functions.
- K Bar graph showing miscibility temperatures of GPMVs isolated from MDCK cells exposed to the indicated conditions. All values represent mean \pm SEM. Data points represent values from biological replicates. Statistical test employed was Student's *t*-test.

making the mTORC1–transcription factor axis less tractable. As an alternative, one could specifically ablate the downstream genes that encode agents of disease. In the case of pH-responsive endolysosomal proteins, dissipation of vesicular acidity may mimic gene ablation. The latter rationale has guided chemotherapeutic strategies that espouse endolysosomal alkalization using chloroquine [12]. However, since many endolysosomal proteins are pH sensitive, neutralizing vesicular acidity could elicit unintended outcomes.

Targeting endolysosomal genes that are selectively upregulated in a particular type of cancer might be an appropriately nuanced strategy to suppress tumorigenesis. Since principal endolysosomal culprits could vary between cancers, *a priori* knowledge of gene expression profiles in different cancers would be needed. To test this idea, we analyzed patterns of endolysosomal gene expression using oncogenic *HRAS*-driven BLCA, HNSC, and THCA as a model. Network analyses of overexpressed endolysosomal genes, many of which are under the control of Mitf/Tfe3/Tfeb, pointed to an important role for *MCOLN1*. Expression of oncogenic *HRAS* was both necessary and sufficient for eliciting the *MCOLN1* overexpression in the human cancer cell lines we examined. Consistent with increased *MCOLN1* expression, TRPML1-mediated endolysosomal Ca^{2+} release was elevated in cancer cells with oncogenic *HRAS* mutations. Interestingly, expression of the activated variant of *Drosophila Ras* also led to increased expression of the *MCOLN1* ortholog, *trpml*, indicating an evolutionarily conserved role for RAS–ERK signaling in the expression of TRPMLs. Furthermore, *MCOLN1* knockdown diminished the proliferation of cancer cells that expressed oncogenic *HRAS*. Pharmacological inhibition of TRPML1—directly with ML-SI1 or indirectly by blocking $\text{PI}(3,5)\text{P}_2$ synthesis—also restricted the proliferation of human cancer cells carrying oncogenic *HRAS* mutations. Increased cell proliferation and RAS–ERK signaling observed in *Drosophila* cells expressing activated variants of *dRas* or human *HRAS* were significantly attenuated in animals lacking the TRPML1 ortholog. Interestingly, ectopic overexpression of *MCOLN1* in oral

cancer cells that were wild type for *HRAS* led to an increase in cell proliferation, which raises the intriguing notion that oncogenic *HRAS* drives cancer cell proliferation in part by upregulating *MCOLN1* expression.

Neither *MCOLN1* knockdown nor TRPML1 inhibition affected the proliferation of cells without oncogenic *HRAS*. We demonstrated the selective vulnerability of *HRAS*-driven cancer cells to decreased TRPML1 function in bioinformatic analyses of patient prognosis, two separate oral cancer cell lines, and a bladder cancer cell line. Stratification of HNSC and BLCA patients with oncogenic *HRAS* mutations on the basis of *MCOLN1* or *MTM1* expression revealed that higher *MCOLN1* or lower *MTM1* expression correlated with poorer patient prognosis. The correlations between *MCOLN1* and *MTM1* expression and patient survival were not observed in HNSC or THCA patients that were wild type for *HRAS*.

From a mechanistic standpoint, we found that inhibition of TRPML1 diminished the formation of $\text{HRAS}^{\text{G}12\text{V}}$ nanoclusters and the levels of the protein in the plasma membrane. Whereas nanoclustering of the wild-type protein was also diminished upon TRPML1 inhibition, we did not detect a decrease in the plasma membrane levels of HRAS^{WT} by ML-SI1. Given that both plasma membrane localization and nanoclustering affect the signal output of *HRAS* [48–50], our data suggest that the selective loss of $\text{HRAS}^{\text{G}12\text{V}}$ from the plasma membrane underlies the specificity of TRPML1 (please refer to model in Fig 6H). The effects of *MCOLN1* knockdown or TRPML1 inhibition on $\text{HRAS}^{\text{G}12\text{V}}$ clustering and localization could be restored by the ectopic addition of cholesterol. Indeed, inhibition of TRPML1 decreased cellular cholesterol levels, especially at the plasma membrane, due to the combined inhibition of cholesterol de-esterification and recycling of cholesterol-laden endolysosomal vesicles back to the membrane. The necessity for cholesterol in the proliferation was further demonstrated by application of TRPML1-independent cholesterol depletion agents.

This study adds to the growing body of knowledge regarding endolysosomal proteins in oncogenesis. A recent study reported that increased expression of a TRPML1 paralog, TRPML2, supports tumorigenesis in glioma [64]. We also found that the gene encoding TRPML2 is slightly elevated in HN31 cells and plays a minor role in cancer cell proliferation. Other endolysosomal transporters and channels have also been implicated in cancer progression [65]. Our findings are also reminiscent of the reports that inhibition of lysosomal acid sphingomyelinase attenuates ERK signaling and tumorigenesis [8,10,11]. The overlap in the phenotypes associated with inhibition of acid sphingomyelinase and TRPML1 raises the question of whether these proteins experience functional interdependence. Since activity of TRPML1 is subject to regulation by a diverse group of membrane lipids [30], it is plausible that sphingomyelins influence TRPML1 function. From a therapeutic perspective, it would be worthwhile to assess whether simultaneous inhibition of TRPML1 and acid sphingomyelinase could synergistically deter tumorigenesis. It is also possible that a combinatorial approach of simultaneous inhibition of both proteins could permit usage of subthreshold drug concentrations and thereby minimize the potential side effects associated with the administration of either drug alone. In summary, we anticipate that insights gleaned from this study could be leveraged to design novel anti-cancer therapeutic strategies.

Materials and Methods

Bioinformatic and survival analyses

We examined the expression of 210 endolysosomal genes in BLCA, HNSC, and THCA tumors using TCGA datasets available at the UCSC Xena functional genomics browser (<https://xenabrowser.net>). We obtained mRNA seq counts for each gene in tumors bearing oncogenic *HRAS* mutations (missense mutations at codons 12, 13, 61, and 117) and matched normal tissues. We calculated the Z-scores for each gene in every tumor using the formula:

$$Z(\text{gene, tumor}) = \frac{(\text{mRNA seq counts in tumor}) - \left(\frac{\text{average of mRNA seq counts in}}{\text{normal tissue}} \right)}{\text{standard deviation of mRNA seq counts in normal tissue}}$$

After calculating individual Z-scores by comparing tumors and matched normal tissues, we combined the Z-values for further analyses.

To evaluate correlated patterns of gene expression in tumor samples, we generated a gene-by-gene matrix comprised of Pearson's coefficients of correlation between Z-scores. We performed unsupervised hierarchical clustering using ClustVis (<https://biit.cs.ut.ee/clustvis/>) [66]. The parameters used for clustering were as follows: (i) no row centering; (ii) no scaling of data; (iii) average linkage method; and (iv) correlation distance metric. Tree ordering of both rows and columns was on the basis of cluster tightness. We separated rows and columns on the basis of tree ordering to permit visualization of cluster boundaries.

To analyze network topology, we used CytoScape. For these analyses, gene names were network nodes and Pearson's correlations of gene expression represented the edge values. To analyze

the network, we treated it as undirected. The network shown in Fig 1G was generated using the "Attribute Circle Layout" on the basis of closeness centrality. The closeness centrality scores were used to rank the endolysosomal genes to generate the GSEA dataset. The nominal *P* and FDR *q* values were obtained after running the "GSEAPreranked" algorithm using the following parameters: (i) number of permutations = 1,000; (ii) enrichment statistic = weighted_p2; and (iii) normalization mode = meandiv.

For survival analyses, we separated the high and low expressors for each gene into the top and bottom 50% on the basis of Z-scores. Subsequently, we used the log-rank (Mantel-Cox) test to determine the *P*-values for each gene.

Cell culture

All cell lines were maintained at 37°C under 5% CO₂. We cultured MDCK and UMCC-22A cells in DMEM containing GlutaMAX (Gibco) that was supplemented with 10% FBS, 2 mM L-glutamine (Invitrogen), and penicillin–streptomycin. We cultured HN31, HT1197 (obtained from ATCC), and T24 (obtained from ATCC) cells in DMEM high glucose media (Fisher Scientific) supplemented with 10% FBS, 2 mM L-glutamine (Invitrogen), penicillin–streptomycin, non-essential amino acids, pyruvate, and vitamins (all from Fisher Scientific). For the experiments involving drug treatment, we added DMSO (vehicle) or the drugs directly to the culture media.

Endolysosomal gene expression analyses

To evaluate the expression of endolysosomal genes, we used the primer sets indicated below. For performing RT-qPCR, we first extracted RNA using the RNeasy Mini Kit (Qiagen) as per the manufacturer's protocol. After quantification of RNA, we generated cDNA using High Capacity cDNA Reverse Transcription Kit (Applied Biosystems) as per the manufacturer's protocol. We performed RT-qPCR using SYBR Green JumpStart Taq ReadyMix (Sigma) as per the manufacturer's protocol.

CTSA:

Forward: 5'-CAGGCTTTGGTCTTCTCTCCA-3'

Reverse: 5'-TCACGCATTCCAGGTCTTTG-3'

CTSD:

Forward: 5' ACTGCTGGACATCGCTTGCT-3'

Reverse: 5'-CATTCTCACGTAGGTGCTGGA-3'

GAPDH:

Forward: 5'-GAAGGTGAAGGTCGGAGTC-3'

Reverse: 5'-GAAGATGGTGATGGGATTTC-3'

GBA:

Forward: 5'-CCAAGCCTTTGAGTAGGGTAAG-3'

Reverse: 5'-CCCGTGTGATTAGCCTGGAT-3'

HEXA:

Forward: 5'-CAACCAACACATTCTTCTCCA-3'

Reverse: 5'-CGCTATCGTGACCTGCTTTT-3'

LAMP1:

Forward: 5'-ACGTTACAGCGTCCAGCTCAT-3'

Reverse: 5'-TCTTTGGAGCTCGCATTGG-3'

MCOLN1:

Forward: 5'-CTGGTGGTCACGGTGCAG-3'

Reverse: 5'-CTGCTCCCGCGTGTAGG-3'

MCOLN2:

Forward: 5'-CGGCAGCCTTATCGTTTTCC-3'

Reverse: 5'-GCCATTGCATTTCTGACGGT-3'

MCOLN3:

Forward: 5'-TCTCCTCCCGTCTGACTCTG-3'

Reverse: 5'-CAGGATCTGCCATCTCTGGG-3'

MITF:

Forward: 5'-GAAATCTTGGGCTTGATGGA-3'

Reverse: 5'-AGGAGTTGCTGATGGTGAGG-3'

TFEB:

Forward: 5'-CCAGAAGCGAGAGCTCACAGAT-3'

Reverse: 5'-TGTGATTGTCTTTCTTCTGCCG-3'

TFE3:

Forward: 5'-AGGATCAAAGAGCTGGGCAC-3'

Reverse: 5'-CCGGCTCTCCAGGTCTTTG-3'

Drosophila trpml:

Forward: 5'-ACGCGAATGTAAGCCGATCT-3'

Reverse: 5'-GGTAGTCGCTCACACACCTC-3'

Drosophila act5C:

Forward: 5'-CGTCGACCATGAAGATCAAG-3'

Reverse: 5'-TTGGAGATCCACATCTGCTG-3'

Ca²⁺ imaging

Cells were trypsinized and seeded onto glass-bottom dishes (*In vitro* Science). The following day, cells were loaded with 10 μ M fura-2-AM (Invitrogen) in culture medium for 1 h. Subsequently, the medium with fura-2-AM was replaced with 150 μ L of bath solution (125 mM NaCl, 5 mM KCl, 10 mM MgSO₄, 10 mM KH₂PO₄, 1 mM CaCl₂, 5.5 mM glucose, and 5 mM HEPES in pH 7.4). Next, dishes containing the cells were mounted on Tie wide-field fluorescence imaging system (Nikon). After baseline fluorescent responses were acquired for ~1.5 min, 50 μ L of bath solution was pipetted out from the dishes to dilute MLSA-1 (Tocris) and GPN (Cayman) and added back to the bath in dishes. Fura-2 signals were recorded by 340/380 nm excitation and 510 nm emission using NIS Elements imaging software (Nikon).

Analyses of cell proliferation

Cell proliferation was determined using two independent assays: CyQuant proliferation assay (ThermoFisher) and WST-1 (4-(3-(4-iodophenyl)-2-(4-nitrophenyl)-2H-5-tetrazolio)-1,3-benzene disulfonate, Roche Applied Sciences) colorimetric assay. For both assays, cells were seeded onto 96-well plates at the density of 10⁴ cells/well and allowed to adhere for 12–24 h at 37°C in a humidified atmosphere of 5% CO₂. Subsequently, fresh growth medium that was supplemented by DMSO or drug as needed was added. After incubation of the cells for the desired durations, cell numbers were determined as per the manufacturer's protocols. Absorbance was measured using a microplate ELISA reader (Cytation 5, BioTek) at 450 nm. Cell proliferation was analyzed by comparing the absorbance values of the samples after background subtraction. All experiments were conducted in eight wells for each condition (technical replicates) and replicated at least three times (biological replicates).

To quantify the effects of β -cyclodextrin and statins on cell proliferation, we cultured the cells in varying concentrations of the drugs for 24 h. For β -cyclodextrin, we applied the drug for 3 h in full growth medium after which the medium was replaced with normal

growth medium. Cells were cultured in the indicated concentrations of statins. To determine the K_i values, we used the Hill input function for a repressor:

$$f(X) = \frac{\beta}{1 + \left(\frac{X}{K_i}\right)^n}$$

This equation was modified to:

$$\frac{1}{f(X)} = \frac{1}{\beta} + \frac{1}{\beta K_i^n} X^n$$

The parameter $f(X)$ was the relative change in cell numbers normalized to the sample with no drug (%), β was the maximal value of $f(X)$ (100%), X was the drug concentration, and n was the Hill coefficient, which was determined empirically by assessing linear fit of the curves generated by plotting $1/f(X)$ against X^n . For β -cyclodextrin, Hill coefficient = 4 (Fig EV5B). For statins, we used the Hill coefficient values of 2 and 5 for HN31 cells and HN31 variants stably expressing *HRAS* shRNA, respectively.

CAM xenografts

Fertilized and specific pathogen-free chicken eggs were purchased from Charles River (Norwich, Connecticut). The chick chorioallantoic membrane (CAM) was accessed and prepared as described previously [37]. On embryonic day 7, the eggs were inoculated with 10⁶ HN31 cells per egg. Three groups of eggs were topically treated on days 1 and 3 after inoculation with 100 μ L of DMSO or ML-SI1 at the concentrations of 10 μ M or 30 μ M. On the 4th or 7th day after inoculation, eggs were humanely euthanized via hypothermia as per American Veterinary Medical Association (AVMA) guidelines (<https://www.avma.org/KB/Policies/Pages/Euthanasia-Guidelines.aspx>). The tumors were excised and fixed in 10% formalin followed by paraffin embedding. Slides made from these blocks were stained with hematoxylin and eosin, and anti-Ki67 antibody (MIB-1, Biocare, Pacheco, CA, USA). The HN31 cell nuclei in the sections can be easily distinguished from the host cell nuclei due to the significantly larger size of the former. For quantification, we counted the numbers of Ki67-positive and Ki67-negative cells in 8–10 fields (using a 10 \times objective) per slide. These numbers allowed us to calculate the fraction of Ki67 nuclei as well as the total number of nuclei per field. Each slide was from a different egg, and the number of these is indicated as data points in the bar graphs.

Gene knockdown by RNA interference

The siRNA sequences used for targeted silencing of human *MCOLN1*, *MITF*, and *TFEB* were designed as described previously [67–69] and custom synthesized as ON-TARGET plus constructs by Sigma-Aldrich. The following sequences were used:

MCOLN1—5'-CCCACATCCAGGAGTGTA-3'

MITF—5'-AGCAGUACCUUUCUACCACTT-3'

TFEB—5'-CCGCCTGGAGATGACCAACAA-3'

Control siRNA (SIC001, Sigma-Aldrich) was used as a negative control. Six-well plates were transfected using X-tremeGENE 9 DNA

Transfection Reagent (Roche). Transfections were performed as described by the manufacturer's protocol. All knockdowns were confirmed by RT-qPCR. The shRNA sequences used were as follows:

MCOLN1:

Target sequence 1: 5'-GCCTGTTCTCGCTCATCAATG-3'

Target sequence 2: 5'-CGTCCTGATCAGTTTGACAA-3'

MCOLN2:

5'-CCGGGCATAGCCAGTGGGATAAATACTCGAGTATTTATCCCACTGGCTATGCTTTTTTG-3'

MCOLN3:

5'-CCGGCTGGCATGTATCTGGATCAATCTCGAGATTGATCCAGATACATGCCAGTTTTTG-3'

VAC14:

5'-CCGGTCCAGATCTGGGTGACAATGCTCGAGCATTGTCACCCAGGATCTGGATTTTTTG-3'

The control shRNA was SHC002—non-target shRNA.

We produced lentiviral particles with a 3rd generation system and used HEKT 293T cell for packaging. Briefly, one day before transfection, we seeded HEKT 293T cells in full growth media into 6-well plates at the appropriate density to achieve ~60% confluency at the time of transfection. We added 10 µg of total DNA per transfection (shRNA-containing vector = 1.6 µg, pMDLg/pRRE = 4 µg, pRSV-Rev = 2 µg, pMD2.g + 2.4 µg) and used a 4:1 ratio of XtremeGENE 9 DNA Transfection Reagent (Roche). We incubated (37°C, 5% CO₂) the transfected HEKT 293T cells for 18 h before adding media with high serum (DMEM+30% FBS). We incubated the cells for 24 h before harvesting the lentivirus-containing media. High serum growth media was replaced, and we harvested the lentivirus a second time after an additional 24-h incubation.

For transduction, we treated the cells with lentivirus-containing media (volume of lentivirus-containing media added made up no more than 1/3 of total media volume) and 8 µg/ml of hexadimethrine bromide (Sigma) for 6 h. We subsequently removed the treatment media and replaced it with full growth media. We allowed the cells to incubate (37°C, 5% CO₂) for at least 24 h before adding puromycin-containing media (2 µg/ml) for selection of cells expressing shRNA.

Western blotting

When generating cellular extracts for Western blotting, we harvested cells in a lysis buffer consisting of 10% NP40, 1 M Tris (pH 7.5), 5 M NaCl, 0.5 M MgCl₂, 0.5 M EGTA (pH 8.0), 5% NaF, Aprotinin (1 mg/ml), 50 mM Na₃VO₄, Leupeptin (1 mg/ml), and 1 M DTT. We loaded cell or *Drosophila* extracts onto 4–20% gradient Tri-glycine gels (Bio-Rad) for SDS-PAGE. After transfer to nitrocellulose membranes, the blots were blocked using the Odyssey blocking buffer (LI-COR Biosciences) followed by incubation with primary antibodies and secondary antibodies described below. All blots were imaged using the Odyssey imaging platform (LI-COR Biosciences). For quantification, we determined band intensities using ImageJ (NIH). When probing the blots with antibodies from the same species, we stripped the blots using the NewBlot™ nitrocellulose stripping buffer as per the manufacturer's instructions (LI-COR Biosciences). All antibody incubations were performed in the Odyssey blocking buffer (LI-COR Biosciences).

Primary antibodies used were rabbit anti-TFEB (Bethyl laboratories) [26], rabbit anti-pERK (Cell Signaling), rabbit anti-ERK (Cell Signaling), and mouse anti-β-tubulin (E7, DSHB). Secondary antibodies used were 680LT anti-rabbit and IRDye 800CW anti-mouse (LI-COR Biosciences).

Drosophila husbandry and stock generation

We reared *Drosophila* on standard fly food (1 l of food contained: 95 g agar, 275 g Brewer's yeast, 520 g of cornmeal, 110 g of sugar, 45 g of propionic acid, and 36 g of Tegosept) as described previously [70]. The fly lines used in these studies were Oregon R, *repo-GAL4* [71], *UAS-mcd8GFP* [72], *UAS-dRas^{V12}* and *he-GAL4* [73], *cg-GAL4* [74].

To generate the *UAS-HRAS^{G12V}* flies, the DNA sequence encoding GFP- and HA-tagged human *HRAS^{G12V}* was PCR-amplified using the primers: forward—ATGGTGAGCAAGGGCGAGGAG; reverse—TTAGGAGAGCACACTTGCAGC. Amplified fragments were subcloned into *pUAS-attB* vector using the In-fusion cloning kit (Clontech). The resulting construct, *pUAS-GFP-HA-HRAS^{G12V}*, was inserted into a *Drosophila* 2nd chromosomal docking site carrying *PBac{y⁺-attP-3B}VK00001*.

Experiments using *Drosophila*

We established crosses with adults of the appropriate genotypes in vials placed in an incubator maintained at 25°C. After clearing the parental adults within a week of setting up crosses, we isolated wandering 3rd-instar larvae from the vials for further analyses. For the experiments involving determination of glial cell volumes, we filleted and fixed the larvae expressing membrane bound GFP and/or *dRas^{V12}* in control or *trpml¹* larvae using PBS + 4% paraformaldehyde for 30 min. After washing the fillets in PBS (3×), we placed the samples in VECTASHIELD mounting media containing DAPI (Vector labs). We imaged the samples using a Nikon A1 confocal microscope using a 20× air objective, with the Z plane thickness set to 1 µm. Subsequently, we generated 3D reconstructions of the larval brains expressing GFP in glia and determined the volume of these reconstructions using ImageJ (NIH).

For analyzing larval macrophages, we tore the body walls of 3rd-instar larvae in depression slides containing 2× Laemmli buffer to simultaneously release and solubilize the cells. We dissected larval fat bodies in PBS in depression slides, after which we removed the PBS and added 2× Laemmli buffer to solubilize the samples.

EM-univariate spatial analysis

The Ripley's univariate K-function analysis tests the null hypothesis that all points with a selected 2D area are distributed randomly [43,47]. We seeded MDCK cells stably expressing GFP-HRAS^{G12V} on pioloform- and poly-L-lysine-coated gold EM grids to a confluent monolayer. Next, we fixed intact basolateral plasma membrane sheets from the MDCK cells attached to the EM grids with 4% paraformaldehyde (PFA) and 0.1% glutaraldehyde, followed by immunolabeling with 4.5 nm gold nanoparticles conjugated to anti-GFP antibody. Finally, we negative-stained the grids with uranyl acetate and embedded in methyl cellulose. Gold nanoparticles on the intact basal plasma membrane sheets were imaged using TEM at

100,000× magnification. X, Y coordinates of every gold particle within a selected 1 μm^2 plasma membrane area were assigned via ImageJ.

Nanoclustering of the gold nanoparticles within the same 1- μm^2 plasma membrane area was calculated via the K-function univariate analysis:

$$K(r) = An^{-2} \sum_{i \neq j} w_{ij} 1(\|x_i - x_j\| \leq r)$$

$$L(r) - r = \sqrt{\frac{K(r)}{\pi}} - r$$

where $K(r)$ = the univariate spatial distribution analysis for n gold particles within an intact plasma membrane area of A ; r is the length scale between 1 and 240 nm; $\|\cdot\|$ is the Euclidean distance, which possesses a value of 1 when $\|x_i - x_j\| \leq r$ or a value of 0 when $\|x_i - x_j\| > r$. The parameter w_{ij}^{-1} , which is used for an unbiased edge correction, defines the fraction of the circumference of a circle with the center at x_i and radius $\|x_i - x_j\|$. Monte Carlo simulations estimate the 99% confidence interval (99% CI), which is used to normalize $L(r) - r$ linearly transformed from $K(r)$. A $L(r) - r$ value of 0 indicates gold distribution is completely random. A $L(r) - r$ value above the 99% CI of 1 indicates statistical clustering.

For each condition, at least 15 plasma membrane sheets were imaged and analyzed. We use bootstrap tests to compare our calculated point patterns to 1,000 bootstrap samples to evaluate the statistical significance between drug-treated and drug-untreated groups as described [75].

Lipid add-back experiments

For the experiments involving cholesterol or PS add-back, we transferred lipids dissolved in chloroform at 5 mg/ml (for a final working concentration of 10 μM) to a glass vial using a Hamilton syringe. We placed the vials under vacuum overnight to completely evaporate chloroform. The dried lipid film was then re-hydrated with cell culture medium, which was sonicated for 20 min to generate small unilamellar vesicles for easy incorporation into cells. We incubated the cells in medium containing the lipid vesicle suspension for 1–3 h to allow incorporation of the exogenous lipids. Successful incorporation of the exogenous lipids was validated using immunogold labeled GFP-tagged specific lipid-binding domains in EM, assessment of fluorescence upon addition of fluorescent lipids, and lipidomic analyses [47,76].

Cholesterol estimation

For cholesterol estimation, we solubilized of 20–30 *Drosophila* larval brains or human cancer cells in 200 μl of extraction solution (chloroform: isopropanol: NP-40 = 7:10:0.1). After centrifugation at 15,000 g for 10 min, the liquid phase was isolated and dried—first at 55°C and then under a vacuum. We assayed the total lipid extract using the Total Cholesterol and Cholesteryl Ester Colorimetric/Fluorometric Assay Kit (BioVision) as per the manufacturer's instructions. For each experiment, we prepared a series of cholesterol standards (0, 0.1, 0.2, 0.4, and 0.5 $\mu\text{g}/\text{well}$). A 96-well plate containing the samples mixed with the reaction mixture was

wrapped in aluminum foil and incubated at 37°C for 60 min. Fluorescence signals (excitation/emission = 535/590 nm) were measured by an Infinity M200 plate reader (Tecan). We determined the free cholesterol in each sample using a standard curve.

Transfection and imaging of cultured cells

We seeded MDCK cells stably expressing mCherry-D4H on glass coverslips 15–20 h before transfection with plasmids carrying LAMP1-mGFP. We transfected the cells in serum-free culture medium using X-tremeGENE 9 transfection reagent (Sigma-Aldrich) according to the manufacturer's instructions. 24 h after transfection, we replaced the culture medium with growth medium containing 10% fetal bovine serum.

After drug treatment, we fixed the cells on coverslips using PBS + 4% paraformaldehyde for 30 min. After washing off the fixative, we mounted the coverslips in VECTASHIELD mounting media containing DAPI (Vector labs). We imaged the coverslips using a Nikon A1 confocal microscope using a 40× oil objective. We counted the number of mCherry-D4H puncta in Z-projections of confocal images using ImageJ (NIH).

To visualize sphingomyelin, we applied a recombinant fragment of lysenin protein tagged with GFP as described [55]. Briefly, live MDCK cells were incubated with 60 $\mu\text{g}/\text{ml}$ MBP-GFP-lysenin (amino acids 161–297 of full-length lysenin) for 15 min at room temperature in serum-free medium. Subsequently, we fixed cells with 4% paraformaldehyde (PFA). In another set of experiments, we first fixed and permeabilized the cells using 0.05% saponin before incubation with 60 $\mu\text{g}/\text{ml}$ MBP-GFP-lysenin and DAPI for 15 min at room temperature. All samples were then imaged in a Nikon A1 confocal microscope.

Subconfluent (60–70%) cells grown on glass bottom dishes (*In Vitro* Science) were incubated with DMEM supplemented with 10% FBS. One day after seeding, cells treated with DMSO or 10 μM ML-SI1. After 24 h incubation, filipin staining of formaldehyde-fixed cells was performed to assess the effect of manipulations on membrane cholesterol. In brief, cells were fixed in 4% formaldehyde in PBS for 15 min followed by incubation in PBS containing 125 $\mu\text{g}/\text{ml}$ filipin (Sigma-Aldrich) for 30 min at room temperature. All samples were then imaged in a Nikon A1 confocal microscope.

Isolation and analysis of GPMVs

We isolated GPMVs and calculated the miscibility temperature as described [58,59,77]. Briefly, cells were washed with PBS and stained with 5 $\mu\text{g}/\text{ml}$ FAST-DiO (Invitrogen), a green fluorescent lipid dye that strongly partitions to the disordered phase, for 10 min on ice. Then, the cells were washed twice with GPMV buffer (10 mM HEPES, 150 mM NaCl, 2 mM CaCl_2 , pH 7.4) and incubated with 25 mM PFA and 2 mM DTT for 1 h at 37°C to induce GPMV formation. The GPMV-rich suspension was then decanted and placed in a temperature-regulated imaging chamber. GPMVs were imaged from 4°C to 28°C, counting phase-separated and uniform vesicles at each temperature. For each temperature, 25–50 vesicles were counted and the percent of phase-separated vesicles were calculated, plotted versus temperature, and fitted to a sigmoidal curve to determine the temperature at which 50% of the vesicles

were phase-separated (i.e., miscibility temperature), which is demonstrated by the dashed vertical lines in Fig 7J.

Statistical methods and data analyses

Graphs were generated using Prism (GraphPad software). In case of normally distributed data, we determined significance using Student's *t*-tests with Bonferroni post hoc corrections in cases of multiple pairwise comparisons. For data that were not normally distributed, we used Mann-Whitney test. We made corrections for multiple hypotheses testing whenever appropriate. Conventions used for describing significance in the figures were: **P* < 0.05; ***P* < 0.01; ****P* < 0.001; *****P* < 0.0001; n.s., not significant (*P* > 0.05).

Expanded View for this article is available online.

Acknowledgements

We thank Barbara Diaz-Rohrer, Yufang Chao, Shilpa Narayanan, and Dr. Boyun Kim for technical help; the Bloomington *Drosophila* Stock Center for fly stocks; Dr. Jeffrey Myers (MDACC) for providing the oral cancer cell lines; Drs. Jeffrey Chang, Ghislain Breton, and Holger K. Eltzschig for use of equipment, and Drs. Jeffrey Chang and Marco Sardiello for helpful discussions. Confocal and live cell microscopy was performed at the Center for Advanced Microscopy, Department of Integrative Biology & Pharmacology at McGovern Medical School, UTHealth. The CAM xenograft experiments were performed at the "Patient-Derived Xenograft and Advanced *in vivo* Models Core Facility" at Baylor College of Medicine (BCM) with funding from the Cancer Prevention and Research Institute of Texas (CPRIT) grant #170691 and the NCI P30CA125123 Center Grant which supports BCM's Dan L. Duncan Cancer Center shared resources. CAM sections were generated by the Pathology and Histology Core (HTAP) core at BCM (M. "Sayeed" Sayeeduddin, Shahida Salar, Zahida Sayeeduddin, Myoung Kwon, Dr. Patricia Castro, Jami Oritz), which is supported by a P30 Cancer Center Support Grant (NCI-CA125123). This work was supported by a CPRIT grant RP170233 (to J.F.H.); NIH grant R00CA188593 (to K.J.C.); and NIH grants R01NS08130 and R21NS094860, and PENN Orphan Disease Center MBBR-18-132-RAS (to K.V.).

Author contributions

JJ performed the majority of the experiments with help from K-JC, AKN, KNC, COW, MV, SG, NEK, LT, HL, MAR, KMT, YZ, and KV. KV performed the bioinformatic analyses. COW helped with Ca²⁺ imaging and cholesterol measurements. KNC, MAR, and KMT helped with Western blot analyses. MV and AGS performed the CAM assay. NEK helped with the generation of shRNA and stable transfections of cancer cells. LT performed some of the cell staining. SG and IL generated and analyzed GPMVs. K-JC, HL, YZ, and JFH performed and supervised the EM analyses. AKN and DH performed some of the cell proliferation experiments. JJ and KV analyzed the data, and KV wrote the manuscript.

Conflict of interest

The authors declare that they have no conflict of interest.

References

- Simanshu DK, Nissley DV, McCormick F (2017) RAS proteins and their regulators in human disease. *Cell* 170: 17–33
- Cho K, Kasai RS, Park J-H, Chigurupati S, Heidorn SJ, van der Hoeven D, Plowman SJ, Kusumi A, Marais R, Hancock JF (2012) Raf inhibitors target ras spatiotemporal dynamics. *Curr Biol* 22: 945–955
- Kidger AM, Siphthorp J, Cook SJ (2018) ERK1/2 inhibitors: new weapons to inhibit the RAS-regulated RAF-MEK1/2-ERK1/2 pathway. *Pharmacol Ther* 187: 45–60
- Ying H, Kimmelman AC, Lyssiotis CA, Hua S, Chu GC, Fletcher-Sanankone E, Locasale JW, Son J, Zhang H, Colloff JL et al (2012) Oncogenic kras maintains pancreatic tumors through regulation of anabolic glucose metabolism. *Cell* 149: 656–670
- Son J, Lyssiotis CA, Ying H, Wang X, Hua S, Ligorio M, Perera RM, Ferrone CR, Mullarky E, Shyh-Chang N et al (2013) Glutamine supports pancreatic cancer growth through a KRAS-regulated metabolic pathway. *Nature* 496: 101–105
- Kim J, Hu Z, Cai L, Li K, Choi E, Faubert B, Bezwada D, Rodriguez-Canales J, Villalobos P, Lin Y-F et al (2017) CPS1 maintains pyrimidine pools and DNA synthesis in KRAS/LKB1-mutant lung cancer cells. *Nature* 546: 168–172
- Commisso C, Davidson SM, Soydaner-Azeloglu RG, Parker SJ, Kamphorst JJ, Hackett S, Grabocka E, Nofal M, Drebin JA, Thompson CB et al (2013) Macropinocytosis of protein is an amino acid supply route in Ras-transformed cells. *Nature* 497: 633–637
- Cho K, van der Hoeven D, Zhou Y, Maekawa M, Ma X, Chen W, Fairn GD, Hancock JF (2015) Inhibition of acid sphingomyelinase depletes cellular phosphatidylserine and mislocalizes K-Ras from the plasma membrane. *Mol Cell Biol* 36: MCB.00719-15
- Perera RM, Stoykova S, Nicolay BN, Ross KN, Fitamant J, Boukhali M, Lengrand J, Deshpande V, Selig MK, Ferrone CR et al (2015) Transcriptional control of autophagy-lysosome function drives pancreatic cancer metabolism. *Nature* 524: 361–365
- Petersen NHT, Olsen OD, Groth-Pedersen L, Ellegaard A-M, Bilgin M, Redmer S, Ostenfeld MS, Ulanet D, Dovmark TH, Lønborg A et al (2013) Transformation-associated changes in sphingolipid metabolism sensitize cells to lysosomal cell death induced by inhibitors of acid sphingomyelinase. *Cancer Cell* 24: 379–393
- van der Hoeven D, Cho K-J, Zhou Y, Ma X, Chen W, Naji A, Montufar-Solis D, Zuo Y, Kovar SE, Levental KR et al (2017) Sphingomyelin metabolism is a regulator of KRAS function. *Mol Cell Biol* 38: e00373-17
- Mancias JD, Kimmelman AC (2011) Targeting autophagy addiction in cancer. *Oncotarget* 2: 1302–1306
- Morgan MJ, Gamez G, Menke C, Hernandez A, Thorburn J, Gidan F, Staskiewicz L, Morgan S, Cummings C, Maycotte P et al (2014) Regulation of autophagy and chloroquine sensitivity by oncogenic RAS *in vitro* is context-dependent. *Autophagy* 10: 1814–1826
- Sardiello M, Palmieri M, di Ronza A, Medina DL, Valenza M, Gennarino VA, Di Malta C, Donaudo F, Embrione V, Polishchuk RS et al (2009) A gene network regulating lysosomal biogenesis and function. *Science* 325: 473–477
- Martina JA, Diab HI, Lishu L, Jeong-A L, Patange S, Raben N, Puertollano R (2014) The nutrient-responsive transcription factor TFE3 promotes autophagy, lysosomal biogenesis, and clearance of cellular debris. *Sci Signal* 7: ra9
- Ploper D, Taelman VF, Robert L, Perez BS, Titz B, Chen H-W, Graeber TG, von Euw E, Ribas A, De Robertis EM (2015) MITF drives endolysosomal biogenesis and potentiates Wnt signaling in melanoma cells. *Proc Natl Acad Sci* 112: E420–E429
- Palmieri M, Impey S, Kang H, di Ronza A, Pelz C, Sardiello M, Ballabio A (2011) Characterization of the CLEAR network reveals an integrated control of cellular clearance pathways. *Hum Mol Genet* 20: 3852–3866

18. Frasca F, Vella V, Nicolosi ML, Messina RL, Gianì F, Lotta S, Vigneri P, Regalbuto C, Vigneri R (2013) Thyroid cancer cell resistance to gefitinib depends on the constitutive oncogenic activation of the ERK pathway. *J Clin Endocrinol Metab* 98: 2502–2512
19. Lawrence MS, Sougnez C, Lichtenstein L, Cibulskis K, Lander E, Gabriel SB, Getz G, Ally A, Balasundaram M, Birol I et al (2015) Comprehensive genomic characterization of head and neck squamous cell carcinomas. *Nature* 517: 576–582
20. McDaniel AS, Zhai Y, Cho KR, Dhanasekaran SM, Montgomery JS, Palapattu G, Siddiqui J, Morgan T, Alva A, Weizer A et al (2014) HRAS mutations are frequent in inverted urothelial neoplasms. *Hum Pathol* 45: 1957–1965
21. Dong X, Shen D, Wang X, Dawson T, Li X, Zhang Q, Cheng X, Zhang Y, Weisman LS, Delling M et al (2010) PI(3,5)P₂ controls membrane trafficking by direct activation of mucolipin Ca²⁺ release channels in the endolysosome. *Nat Commun* 1: 1–11
22. Sbrissa D, Ikononov OC, Strakova J, Dondapati R, Mlak K, Deeb R, Silver R, Shisheva A (2004) A mammalian ortholog of *Saccharomyces cerevisiae* Vac14 that associates with and up-regulates PIKfyve phosphoinositide 5-kinase activity. *Mol Cell Biol* 24: 10437–10447
23. Ketel K, Krauss M, Nicot A-S, Puchkov D, Wiewer M, Müller R, Subramanian D, Schultz C, Laporte J, Haucke V (2016) A phosphoinositide conversion mechanism for exit from endosomes. *Nature* 529: 408–412
24. Subramanian A, Tamayo P, Mootha VK, Mukherjee S, Ebert BL, Gillette MA, Paulovich A, Pomeroy SL, Golub TR, Lander ES et al (2005) Gene set enrichment analysis: a knowledge-based approach for interpreting genome-wide expression profiles. *Proc Natl Acad Sci USA* 102: 15545–15550
25. Hah JH, Zhao M, Pickering CR, Frederick MJ, Andrews GA, Jasser SA, Fooshee DR, Milas ZL, Galer C, Sano D et al (2014) HRAS mutations and resistance to the epidermal growth factor receptor tyrosine kinase inhibitor erlotinib in head and neck squamous cell carcinoma cells. *Head Neck* 36: 1547–1554
26. Peña-Llopis S, Vega-Rubin-de-Celis S, Schwartz JC, Wolff NC, Tran TAT, Zou L, Xie X-J, Corey DR, Brugarolas J (2011) Regulation of TFEB and V-ATPases by mTORC1. *EMBO J* 30: 3242–3258
27. Promislow DEL (2004) Protein networks, pleiotropy and the evolution of senescence. *Proc Biol Sci* 271: 1225–1234
28. Peng C-C, Chen K-C, Peng RY, Su C-H, Hsieh-Li HM (2006) Human urinary bladder cancer T24 cells are susceptible to the *Anrodia camphorata* extracts. *Cancer Lett* 243: 109–119
29. Szepeshazi K, Schally AV, Keller G, Block NL, Bente D, Halmos G, Szalontay L, Vidaurre I, Jaszberenyi M, Rick FG (2012) Receptor-targeted therapy of human experimental urinary bladder cancers with cytotoxic LH-RH analog AN-152 [AEZS-108]. *Oncotarget* 3: 686–699
30. Shen D, Wang X, Li X, Zhang X, Yao Z, Dibble S, Dong X, Yu T, Lieberman AP, Showalter HD et al (2012) Lipid storage disorders block lysosomal trafficking by inhibiting a TRP channel and lysosomal calcium release. *Nat Commun* 3: 731
31. Berg TO, Strømhaug E, Løvdal T, Seglen O, Berg T (1994) Use of glycyl-L-phenylalanine 2-naphthylamide, a lysosome-disrupting cathepsin C substrate, to distinguish between lysosomes and prelysosomal endocytic vacuoles. *Biochem J* 300(Pt. 1): 229–236
32. Samie M, Wang X, Zhang X, Goschka A, Li X, Cheng X, Gregg E, Azar M, Zhuo Y, Garrity AG et al (2013) A TRP channel in the lysosome regulates large particle phagocytosis via focal exocytosis. *Dev Cell* 26: 511–524
33. Koybasi S, Senkal CE, Sundararaj K, Spassieva S, Bielawski J, Osta W, Day TA, Jiang JC, Jazwinski SM, Hannun YA et al (2004) Defects in cell growth regulation by C_{18:0}-ceramide and longevity assurance gene 1 in human head and neck squamous cell carcinomas. *J Biol Chem* 279: 44311–44319
34. Gómez NM, Lu W, Lim JC, Kiselyov K, Campagno KE, Grishchuk Y, Slaugenhaupt SA, Pfeiffer BA, Fliesler SJ, Mitchell CH (2017) Robust lysosomal calcium signaling through channel TRPML1 is impaired by lysosomal lipid accumulation. *FASEB J* 32: 782–794
35. Jefferies HBJ, Cooke FT, Jat P, Boucheron C, Koizumi T, Hayakawa M, Kaizawa H, Ohishi T, Workman P, Waterfield MD et al (2008) A selective PIKfyve inhibitor blocks PtdIns(3,5)P₂ production and disrupts endomembrane transport and retroviral budding. *EMBO Rep* 9: 164–170
36. Sys GML, Lapeire L, Stevens N, Favoreel H, Forsyth R, Bracke M, De Wever O (2013) The in ovo CAM-assay as a xenograft model for sarcoma. *J Vis Exp* 77: e50522
37. Li M, Pathak RR, Lopez-Rivera E, Friedman SL, Aguirre-Ghiso JA, Sikora AG (2015) The *In Ovo* chick chorioallantoic membrane (CAM) assay as an efficient xenograft model of Hepatocellular carcinoma. *J Vis Exp* 104: e52411
38. Venkatachalam K, Hofmann T, Montell C (2006) Lysosomal localization of TRPML2 depends on TRPML1 and the mucopolidosis-associated protein TRPML1. *J Biol Chem* 281: 17517–17527
39. Tetlow AL, Tamanoi F (2013) The ras superfamily G-proteins. *Enzymes* 33 (Pt. A): 1–14
40. Venkatachalam K, Long AA, Elsaesser R, Nikolaeva D, Broadie K, Montell C (2008) Motor deficit in a *Drosophila* model of mucopolidosis type IV due to defective clearance of apoptotic cells. *Cell* 135: 838–851
41. Feng X, Huang Y, Lu Y, Xiong J, Wong C-O, Yang P, Xia J, Chen D, Du G, Venkatachalam K et al (2014) *Drosophila* TRPML forms PI(3,5)P₂-activated cation channels in both endolysosomes and plasma membrane. *J Biol Chem* 289: 4262–4272
42. Neuman-Silberberg FS, Schejter E, Hoffmann FM, Shilo BZ (1984) The *Drosophila* ras oncogenes: structure and nucleotide sequence. *Cell* 37: 1027–1033
43. Prior IA, Muncke C, Parton RG, Hancock JF (2003) Direct visualization of Ras proteins in spatially distinct cell surface microdomains. *J Cell Biol* 160: 165–170
44. Plowman SJ, Muncke C, Parton RG, Hancock JF (2005) H-ras, K-ras, and inner plasma membrane raft proteins operate in nanoclusters with differential dependence on the actin cytoskeleton. *Proc Natl Acad Sci* 102: 15500–15505
45. Hancock JF, Roy S, Luetterforst R, Harding A, Apolloni A, Etheridge M, Stang E, Rolls B, Parton RG (1999) Dominant-negative caveolin inhibits H-Ras function by disrupting cholesterol-rich plasma membrane domains. *Nat Cell Biol* 1: 98–105
46. Parton R, Hancock JF (2004) Lipid rafts and plasma membrane microorganization: insights from Ras. *Trends Cell Biol* 14: 141–147
47. Zhou Y, Wong C-O, Cho K-J, Van Der Hoeven D, Liang H, Thakur DPP, Luo J, Babic M, Zinsmaier KEE, Zhu MXX et al (2015) Membrane potential modulates plasma membrane phospholipid dynamics and K-Ras signaling. *Science* 349: 873–876
48. Agudo-Ibáñez L, Herrero A, Barbacid M, Crespo P (2015) H-ras distribution and signaling in plasma membrane microdomains are regulated by acylation and deacylation events. *Mol Cell Biol* 35: 1898–1914

49. Prior IA, Harding A, Yan J, Sluimer J, Parton RG, Hancock JF (2001) GTP-dependent segregation of H-ras from lipid rafts is required for biological activity. *Nat Cell Biol* 3: 368–375
50. Hancock JF, Parton RG (2005) Ras plasma membrane signalling platforms. *Biochem J* 389: 1–11
51. Sleat DE, Wiseman JA, El-Banna M, Price SM, Verot L, Shen MM, Tint GS, Vanier MT, Walkley SU, Lobel P (2004) Genetic evidence for nonredundant functional cooperativity between NPC1 and NPC2 in lipid transport. *Proc Natl Acad Sci* 101: 5886–5891
52. LaPlante JM, Sun M, Falardeau J, Dai D, Brown EM, Slaugenhaupt SA, Vassilev PM (2006) Lysosomal exocytosis is impaired in mucopolidosis type IV. *Mol Genet Metab* 89: 339–348
53. Ravi S, Peña KA, Chu CT, Kiselyov K (2016) Biphasic regulation of lysosomal exocytosis by oxidative stress. *Cell Calcium* 60: 356–362
54. Wong C-O, Li R, Montell C, Venkatachalam K (2012) *Drosophila* TRPML is required for TORC1 activation. *Curr Biol* 22: 1616–1621
55. Maekawa M (2017) Domain 4 (D4) of perfringolysin O to visualize cholesterol in cellular membranes—the update. *Sensors (Basel)* 17: E504
56. Drabikowski W, Lagwińska E, Sarzala MG (1973) Filipin as a fluorescent probe for the location of cholesterol in the membranes of fragmented sarcoplasmic reticulum. *Biochim Biophys Acta* 291: 61–70
57. Yamaji A, Sekizawa Y, Emoto K, Sakuraba H, Inoue K, Kobayashi H, Umeda M (1998) Lysenin, a novel sphingomyelin-specific binding protein. *J Biol Chem* 273: 5300–5306
58. Levental I, Grzybek M, Simons K (2011) Raft domains of variable properties and compositions in plasma membrane vesicles. *Proc Natl Acad Sci* 108: 11411–11416
59. Levental I, Byfield FJ, Chowdhury P, Gai F, Baumgart T, Janmey PA (2009) Cholesterol-dependent phase separation in cell-derived giant plasma-membrane vesicles. *Biochem J* 424: 163–167
60. Levental KR, Lorent JH, Lin X, Skinkle AD, Surma MA, Stockenbojer EA, Gorfe AA, Levental I (2016) Polyunsaturated lipids regulate membrane domain stability by tuning membrane order. *Biophys J* 110: 1800–1810
61. Settembre C, Di Malta C, Polito VA, Arcencibia MG, Vetrini F, Erdin S, Erdin SU, Huynh T, Medina D, Colella P et al (2011) TFEB links autophagy to lysosomal biogenesis. *Science* 332: 1429–1433
62. Carreira S, Goodall J, Denat L, Rodriguez M, Nuciforo P, Hoek KS, Testori A, Larue L, Goding CR (2006) Mitf regulation of Dia1 controls melanoma proliferation and invasiveness. *Genes Dev* 20: 3426–3439
63. Medina DL, Di Paola S, Peluso I, Armani A, De Stefani D, Venditti R, Montefusco S, Scotto-Rosato A, Prezioso C, Forrester A et al (2015) Lysosomal calcium signalling regulates autophagy through calcineurin and TFEB. *Nat Cell Biol* 17: 288–299
64. Morelli MB, Nabissi M, Amantini C, Tomassoni D, Rossi F, Cardinali C, Santoni M, Arcella A, Oliva MA, Santoni A et al (2016) Overexpression of transient receptor potential mucolipin-2 ion channels in gliomas: role in tumor growth and progression. *Oncotarget* 7: 43654–43668
65. Grimm C, Bartel K, Vollmar A, Biel M (2018) Endolysosomal cation channels and cancer—a link with great potential. *Pharmaceuticals* 11: 4
66. Metsalu T, Vilo J (2015) ClustVis: a web tool for visualizing clustering of multivariate data using Principal Component Analysis and heatmap. *Nucleic Acids Res* 43: W566–W570
67. Colletti GA, Miedel MT, Quinn J, Andharia N, Weisz OA, Kiselyov K (2012) Loss of lysosomal ion channel transient receptor potential channel mucolipin-1 (TRPML1) leads to cathepsin B-dependent apoptosis. *J Biol Chem* 287: 8082–8091
68. Bourseguin J, Bonet C, Renaud E, Pandiani C, Boncompagni M, Giuliano S, Pawlikowska P, Karmous-Benailly H, Ballotti R, Rosselli F et al (2016) FANCD2 functions as a critical factor downstream of Mitf to maintain the proliferation and survival of melanoma cells. *Sci Rep* 6: 36539
69. Song W, Wang F, Lotfi P, Sardiello M, Segatori L (2014) 2-Hydroxypropyl- β -cyclodextrin promotes transcription factor EB-mediated activation of autophagy. *J Biol Chem* 289: 10211–10222
70. Wong C-O, Gregory S, Hu H, Chao Y, Sepúlveda VE, He Y, Li-Kroeger D, Goldman WE, Bellen HJ, Venkatachalam K (2017) Lysosomal degradation is required for sustained phagocytosis of bacteria by macrophages. *Cell Host Microbe* 21: 719–730
71. Sepp KJ, Schulte J, Auld VJ (2001) Peripheral glia direct axon guidance across the CNS/PNS transition zone. *Dev Biol* 238: 47–63
72. Lee T, Luo L (1999) Mosaic analysis with a repressible cell marker for studies of gene function in neuronal morphogenesis. *Neuron* 22: 451–461
73. Zettervall C-J, Anderl I, Williams MJ, Palmer R, Kurucz E, Ando I, Hultmark D (2004) A directed screen for genes involved in *Drosophila* blood cell activation. *Proc Natl Acad Sci* 101: 14192–14197
74. Asha H, Nagy I, Kovacs G, Stetson D, Ando I, Dearolf CR (2003) Analysis of Ras-induced overproliferation in *Drosophila* hemocytes. *Genetics* 163: 203–215
75. Diggle PJ, Mateu J, Clough HE (2000) A comparison between parametric and non-parametric approaches to the analysis of replicated spatial point patterns. *Adv Appl Probab* 32: 331–343
76. Zhou Y, Prakash P, Liang H, Cho K-J, Gorfe AA, Hancock JF (2017) Lipid-sorting specificity encoded in k-ras membrane anchor regulates signal output. *Cell* 168: 239–251.e16
77. Sezgin E, Kaiser H-J, Baumgart T, Schwille P, Simons K, Levental I (2012) Elucidating membrane structure and protein behavior using giant plasma membrane vesicles. *Nat Protoc* 7: 1042–1051

Expanded View Figures

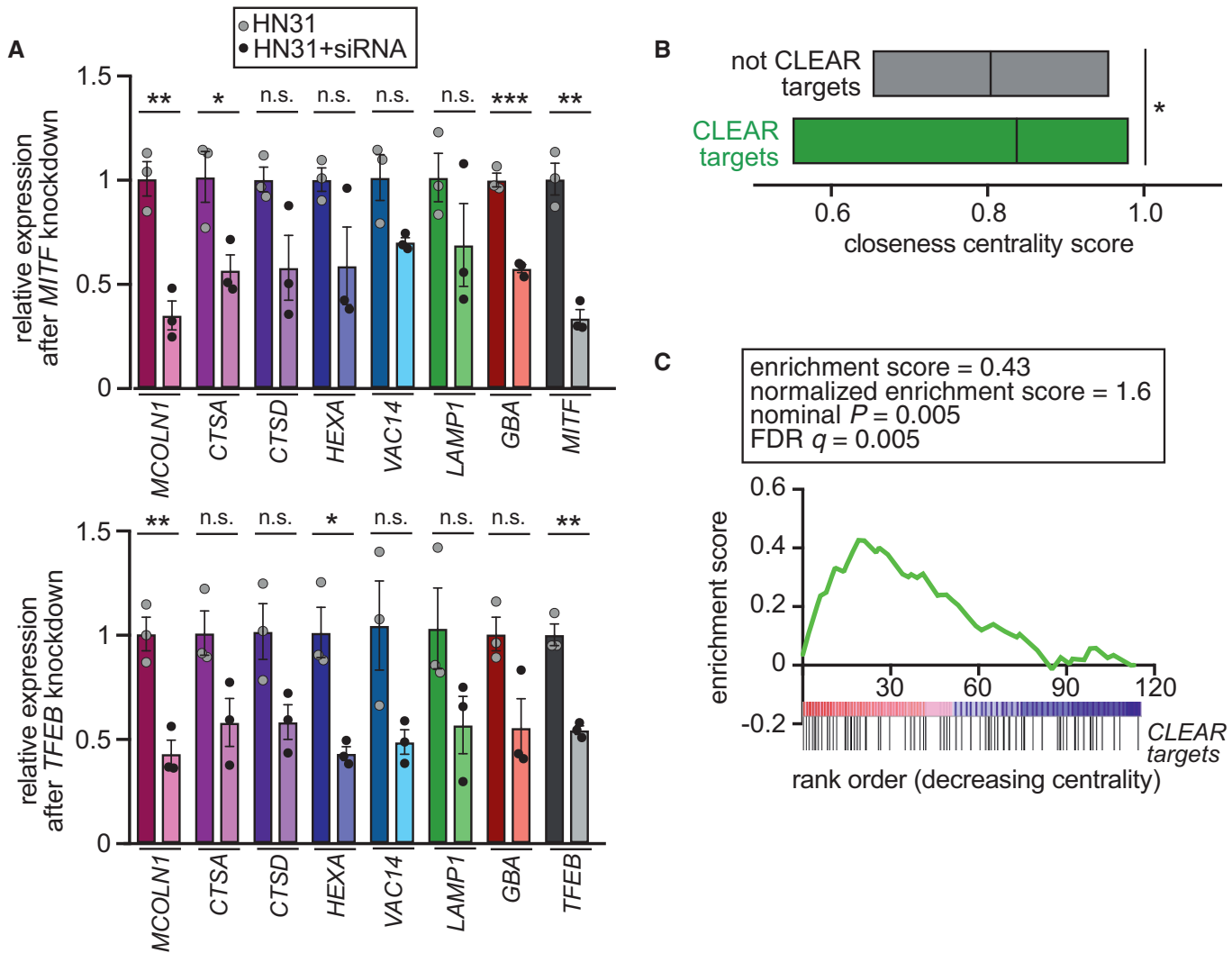


Figure EV1. Correlation between network centrality and membership to the CLEAR family of endolysosomal genes.

A Bar graph showing the relative expression of the indicated genes in the indicated cell types. Bar graphs in the top and bottom panels represent the results of *MITF* and *TFEB* knockdown, respectively. Values were normalized to respective HN31 average and represent mean \pm SEM. Data points represent values from biological replicates. Statistical test employed was Student's *t*-test.

B Bar graph showing that the mean closeness centrality of CLEAR target genes is significantly higher than that of genes that do not belong to the CLEAR network. The lines in the bars represent mean values. Statistical test employed was Student's *t*-test.

C GSEA conducted on endolysosomal genes ranked on the basis of increasing network centrality. Positions of the CLEAR target genes are indicated.

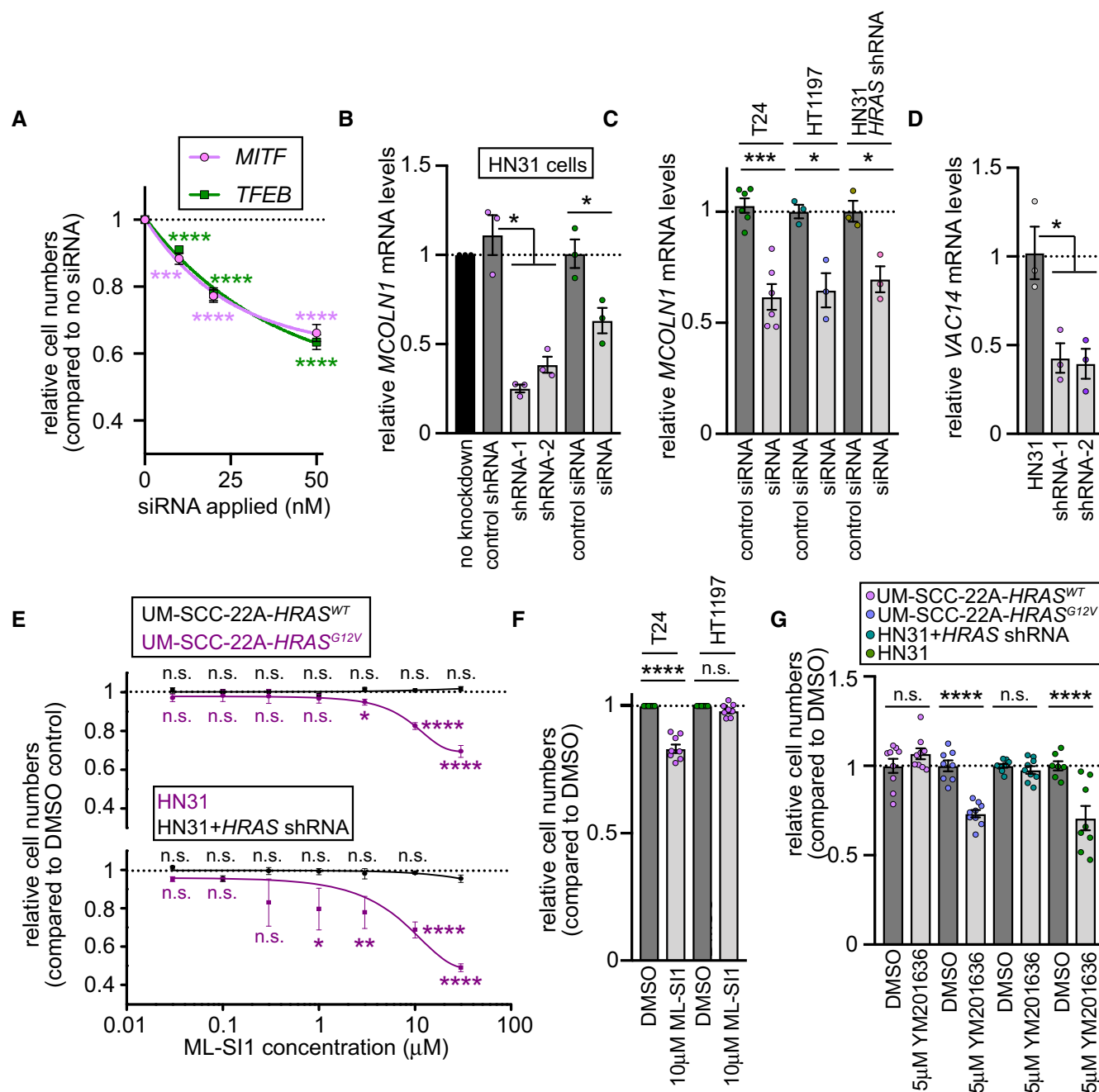


Figure EV2. Roles for the CLEAR network genes in the proliferation of cancer cells with oncogenic *HRAS*.

- A** Graphs showing the relative cell numbers in HN31 cells exposed to the indicated concentrations of siRNAs against MITF and TFEB. All values represent mean \pm SEM, $n = 3$ biological replicates. Statistical tests employed were one-sample *t*-test to examine significance of differences from a hypothetical value of 1.
- B, C** Bar graphs showing relative levels of *MCOLN1* mRNA in the indicated cells types after the indicated perturbations. Values were normalized to “no knockdown” (B) or respective “control siRNA” (C) and represent mean \pm SEM. Data points represent values from biological replicates. Statistical test employed was Student’s *t*-test. Bonferroni *post hoc* correction was applied when for multiple pairwise comparisons in (B).
- D** Bar graph showing relative levels of *VAC14* mRNA in HN31 cells after the indicated perturbations. Values were normalized to HN31 average and represent mean \pm SEM. Data points represent values from biological replicates. Statistical test employed was Student’s *t*-test with Bonferroni *post hoc* correction for multiple pairwise comparisons.
- E** Line graphs showing relative cell numbers in sample of the indicated genotypes treated with indicated ML-SI1 concentrations. All values represent mean \pm SEM. Data points represent values from biological replicates. Statistical test employed was Student’s *t*-test between relative cell numbers at each concentration.
- F, G** Bar graphs showing the relative cell numbers in the indicated cell types following the indicated treatments. All values represent mean \pm SEM. Data points represent values from biological replicates. Statistical test employed was Student’s *t*-test.

Figure EV3. TRPML2 and TRPML3 play minor roles in *HRAS*-driven cancer cell proliferation.

- A Violin plots of average Z-scores of the indicated genes in BLCA, THCA, and HNSC patients with oncogenic *HRAS* mutations. The thick horizontal dashed lines in each sample set represent median; thin dashed lines represent the quartiles; polygons represent density estimates of data and extend to extreme values. Statistical tests employed were 1-sample *t*-test or Wilcoxon signed rank test to examine significance of differences from a hypothetical value of 0.
- B Bar graph showing relative levels of *MCOLN1*, *MCOLN2*, and *MCOLN3* mRNAs in the indicated cells types. All values were normalized to respective "*HRAS* shRNA" average and represent mean \pm SEM. Data points represent values from biological replicates. Statistical test employed was Student's *t*-test.
- C Bar graph showing relative levels of *MCOLN2* and *MCOLN3* mRNAs in HN31 cells after the indicated perturbations. Values were normalized to respective HN31 average and represent mean \pm SEM. Data points represent values from biological replicates. Statistical test employed was Student's *t*-test with Bonferroni *post hoc* correction for multiple pairwise comparisons.
- D Bar graph showing the relative cell numbers in the indicated cell types following the indicated treatments. All values represent mean \pm SEM. Data points represent values from biological replicates. Statistical test employed was Student's *t*-test with Bonferroni *post hoc* correction for multiple pairwise comparisons.

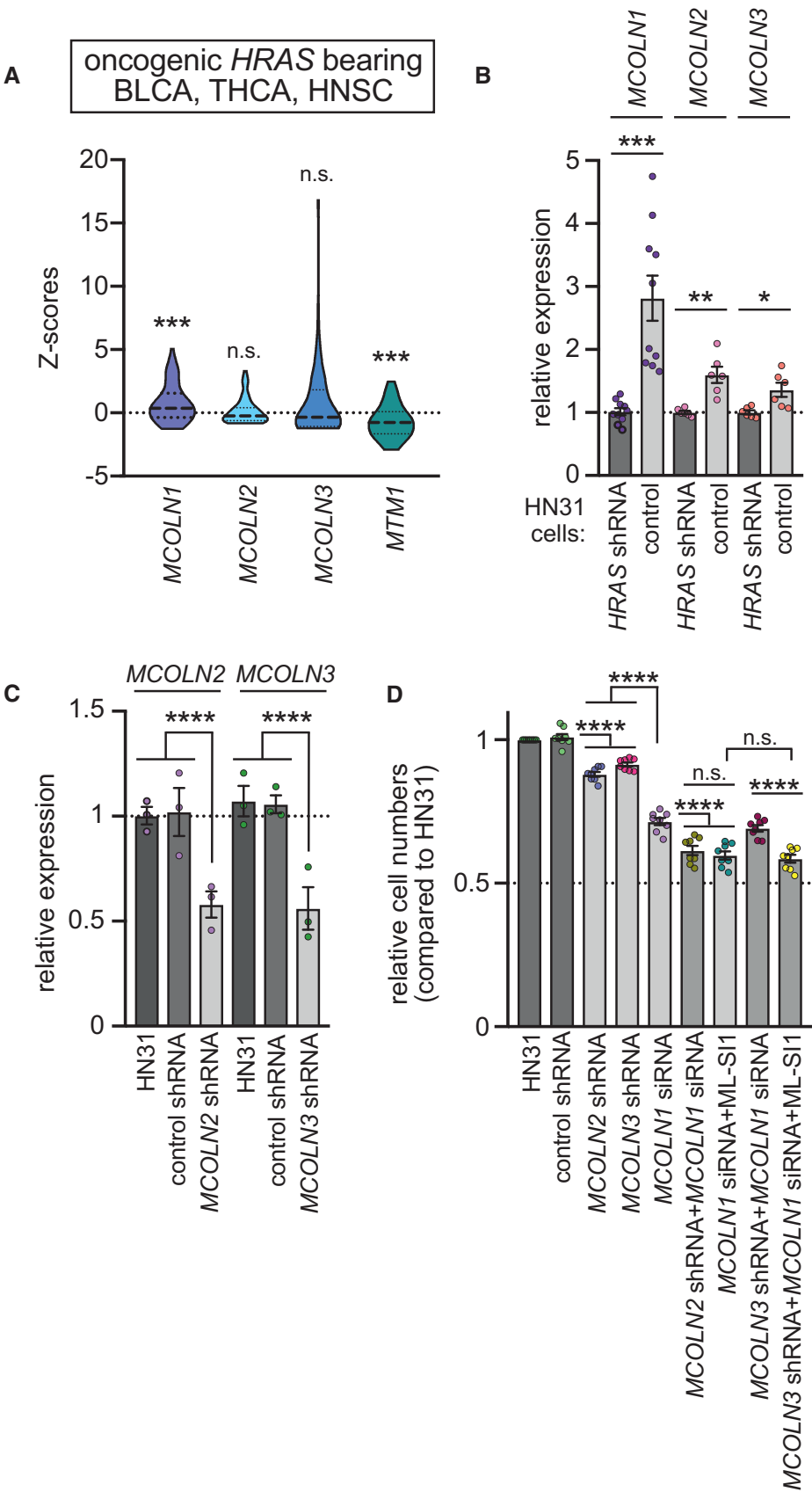


Figure EV3.

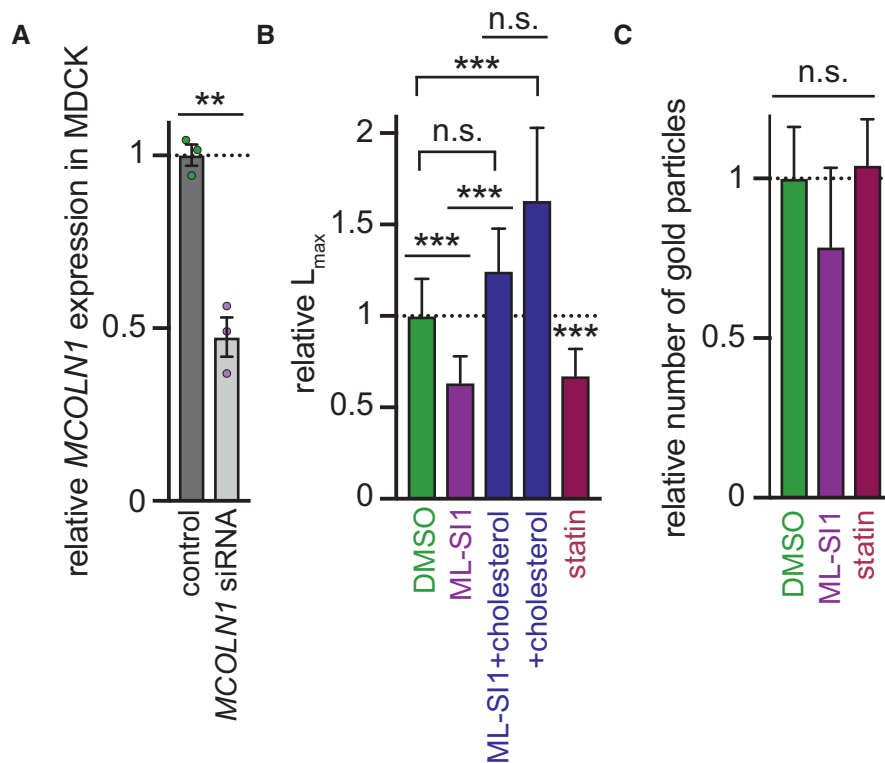


Figure EV4. TRPML1 and cholesterol are required for the clustering of HRAS.

- A Bar graph showing relative levels of *MCOLN1* mRNA in the MDCK cells treated with siRNA against *MCOLN1*. Values are normalized to control average and represent mean \pm SEM. Data points represent values from biological replicates. Statistical test employed was Student's *t*-test.
- B The extent of GFP-HRAS^{WT} nanoclustering quantified as L_{max} in cells exposed to the indicated perturbations. Values were normalized to DMSO average and represent mean \pm SEM ($n \geq 15$ for each condition). Statistical significances of differences were evaluated in bootstrap tests.
- C Bar graph showing GFP-HRAS^{WT} content in the inner leaflet of the plasma membrane is quantified as the number of gold particles per 1 μm^2 region from electron micrographs. Values were normalized to DMSO average and represent mean \pm SEM, $n \geq 15$ for each condition. Statistical test employed was ANOVA.

Figure EV5. Drugs that affect cellular cholesterol levels impact growth of cancer cells with oncogenic HRAS.

- A, C Graphs showing relative cell numbers indicated cell types following application of β -cyclodextrin (A) or statin (C). Cell numbers were assessed after a 24-h period of growth in cultures and normalized to the values obtained in the absence of drug. Values represent mean \pm SEM, $n \geq 3$ biological replicates.
- B *Left*, graph showing that the relative cell numbers of concentration of β -cyclodextrin could be fit to a Hill input function for repressor with Hill coefficient = 4. *Right*, bar graph showing K_i values in the indicated cell types. Values represent mean \pm SEM. Data points represent values from biological replicates. Statistical test employed was Student's *t*-test.
- D Same as the bar graph in (B), but in case of cells treated with statins.
- E Confocal images of control or ML-SI1-treated cells that were exposed to recombinant GFP-lysine. Intracellular GFP-lysine punctae indicate that ML-SI1 led to the internalization of sphingomyelin from the plasma membrane into intracellular vesicles. Scale bar (10 μm) shown in the panel on the top right applies to all panels.

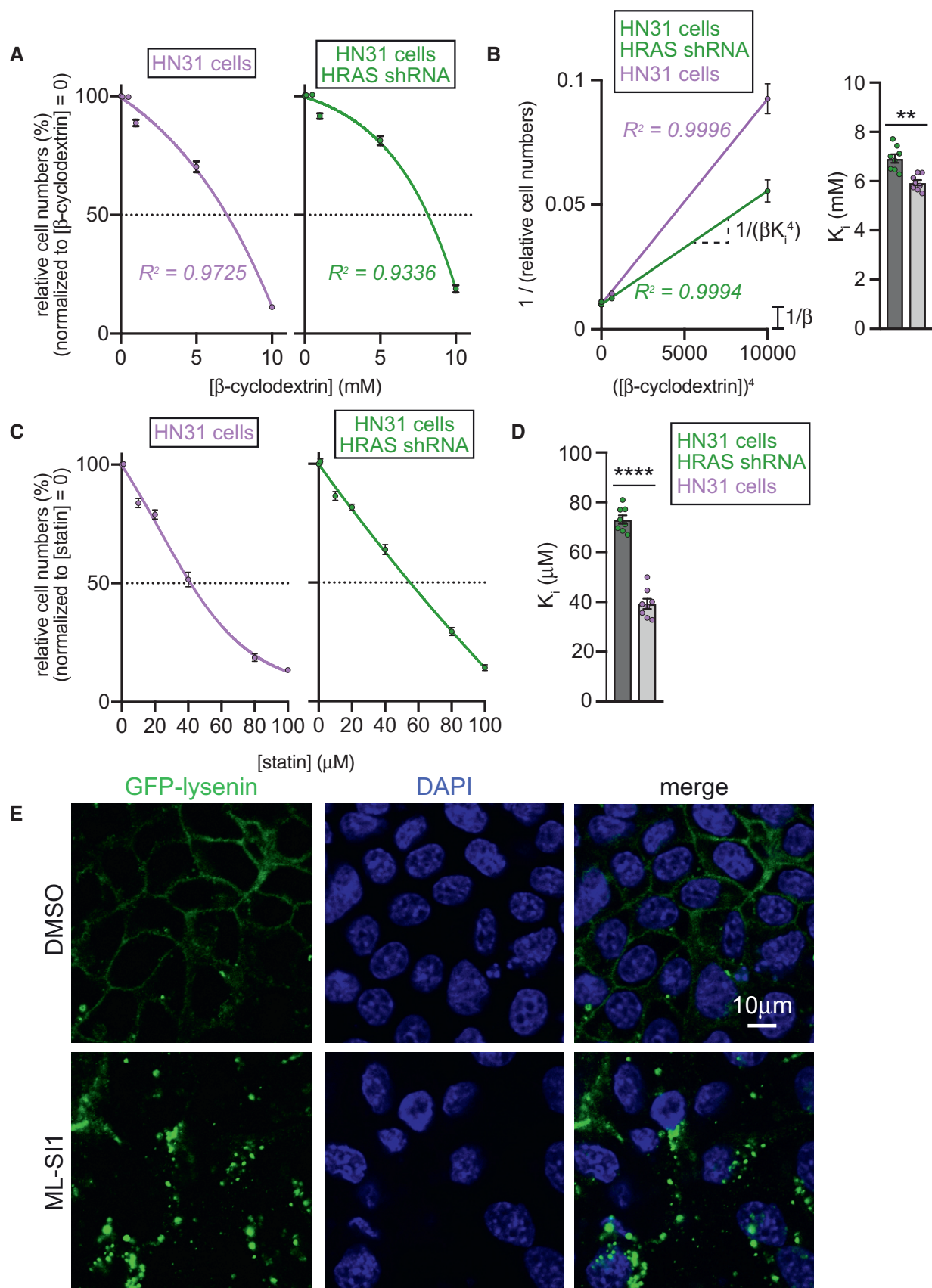


Figure EV5.

Appendix table of contents

Page 1 – Table of contents

Page 2 – Appendix Figure S1

Page 3 – Appendix Figure S2

Page 4– Appendix Figure S3

Page 5 – Appendix Figure S4

singlets

GGH
APCS*cluster 1*

HYAL1
 SIDT2
 DRAM2
 DRAM1
 SYT7
 GAA
 RNASET2
 GIMAP5
 AP1S2
 CTNS
 MPO
 BLOC1S3
 ATP13A2
 SNX8
 ATP6V1E1
 LGMN
 ACP2
 PLA2G15
 TMEM55B
 GBA
 VAC14
 ARSA
 SCAMP3
 STX4
 ARFGAP1
 SPNS1
 NAGPA
 TCIRG1
 NAGA
 TPCN2
 CTSB
 CTSS
 GLB1
 TMEM92
 CREG1
 OSTM1
 SPG21
 CD68
 IL4I1
 IFI30
 LAPTM5
 RNASE6
 CTSZ
 SLC11A1
 HEXB
 PPT1
 CTSF
 SLC17A9
 CTSK
 MAN2B1
 ATP6V1H
 ARPC5
 GLA

cluster 2

IDS
 NCSTN
 PLBD2
 ATP6AP2
 MAN2B2
 CTSC
 NRBF2
 LAMP3
 ZFYVE26
 ATP7B
 MFSD8
 SLC38A9
 GNS
 CTSO
 HPS3
 ARSK
 UVRAG
 SLC37A3
 CLN5
 HPS5
 LIPA
 M6PR
 SNX2
 ATP6V1C1
 KIAA0196
 ATP6V1E2
 SPPL2A
 GALC
 SMCR8
 MFSD1
 PDCD6IP
 VPS35
 VPS8
 SPG20
 NPC1
 SLC36A1
 LAPTM4B
 EPDR1
 CLCN6
 RRAGB
 TMEM55A
 TPP1
 ARSB
 FLCN
 AGA
 PI4K2A
 VPS33A
 ATG3
 HPSE
 SLC31A2

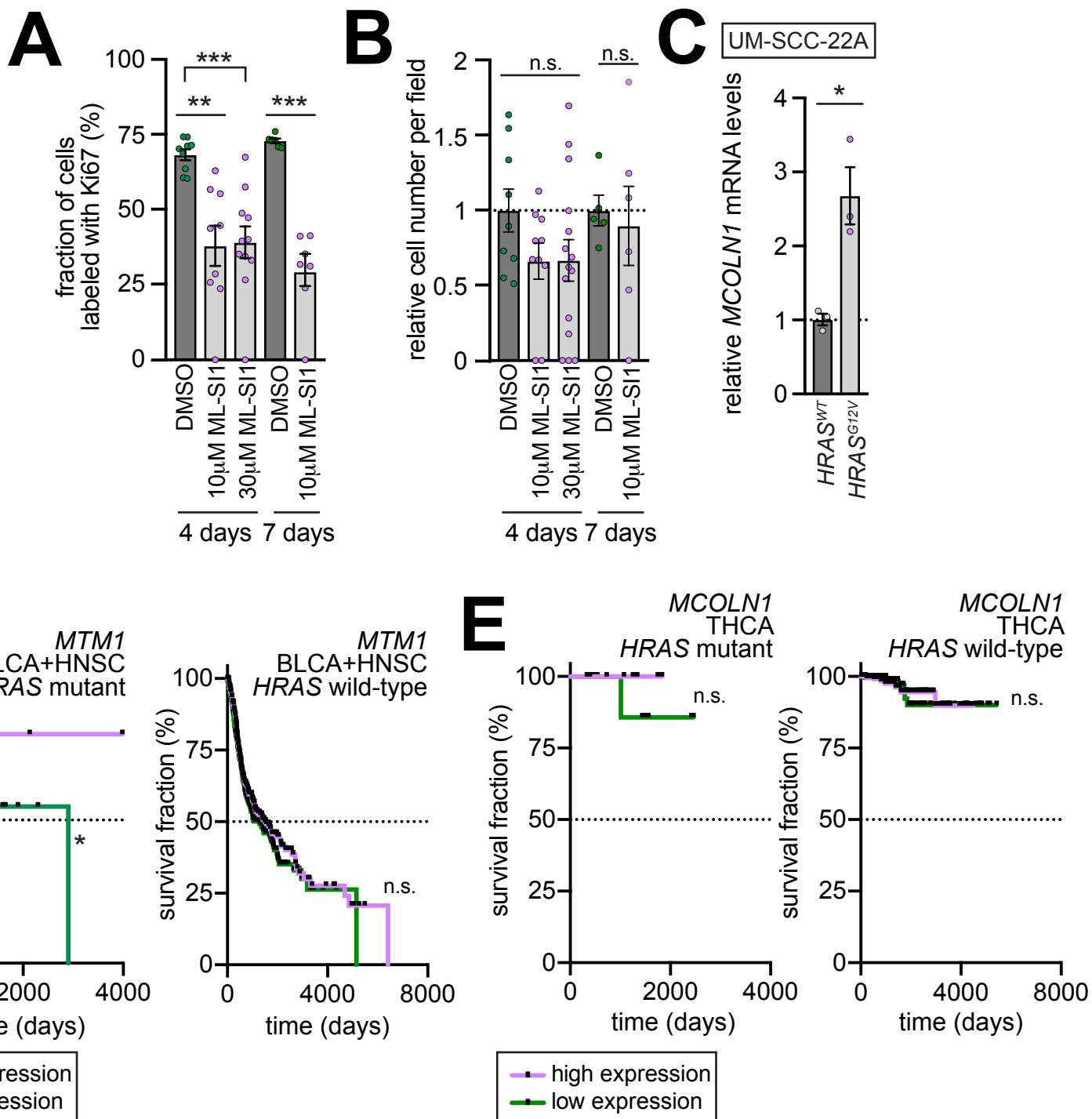
cluster 3

CLN3
 ATP6V0D2
 PSAP
 PPT2
 ATP6V1B1
 PRDX6
 CPA2
 MANBA
 TOM1
 ATP6V1C2
 ATP6V1G1
 ABCB9
 SGSH
 P2RX4
 SCARB1
 SLC26A11
 CLCN7
 SQSTM1
 ATP6AP1
 NEU1
 CTSH
 ATP6V0E2
 PLD3
 CD63
 NPC2
 ATP6V1G3
 SMPD1
 NAAA
 ATP6V0A4
 TMEM8A
 DNASE2
 FUCA1
 ABCD4
 ATP6V0D1
 VPS18
 LAMP1
 GUSB
 HEXA
 NAGLU
 GRN
 MCOLN1
 CTSA
 CTSD
 TMEM9
 AKT1S1
 RNASEK
 ATP6V0B
 CLTA
 ARL8A
 ATP6V1F
 PQLC2
 HPS1
 SERINC2
 DPP7
 WDR45
 ATP6V0C
 SUMF1
 HYAL2
 GNPTG
 IDUA

cluster 4

RAB7A
 RRAGC
 SLC31A1
 LAMP2
 VPS26A
 SNX16
 CLTC
 IGF2R
 ARFGEF2
 LMTK2
 ASAH1
 SCARB2
 CTBS
 MTM1
 PCYOX1
 TMEM106B
 RAB5A
 ATP6V1A
 RAB21
 DIRC2
 STX6
 ENTPD4
 TMEM192
 ATP6V0A2
 CD164
 SLC17A5
 ATP6V0A1
 PLEKHM1
 TMEM127
 SIAE
 ARSG
 LMBRD1
 DPP4
 LPO
 VPS11
 GPR137B
 RRAGD
 TMEM74
 ATP6V1B2
 ATP6V1D
 ATP6V1G2
 ABCB6
 HGSNAT
 ABCA2
 SCPEP1

Appendix Figure S1. List of genes that belong to the clusters shown in Fig 1. The order of the genes in each cluster is the order in which those genes appear on the dendrogram. GGH and APCS do not belong to any of the clusters.



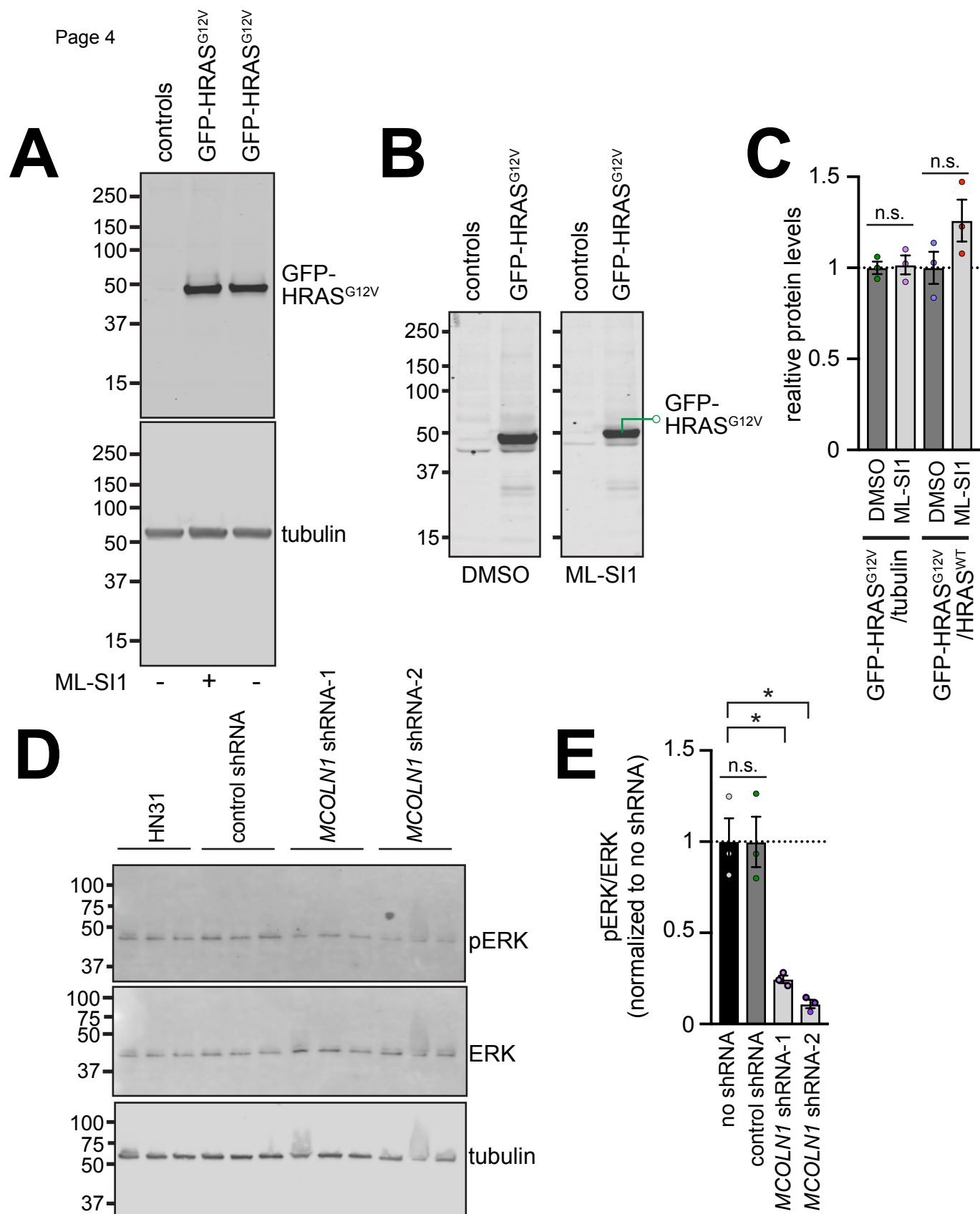
Appendix Figure S2. (A-B) Bar graphs showing fraction **(A)** and total number **(B)** of Ki67 labeled nuclei in HN31 cells exposed to DMSO or the indicated concentrations of ML-SI1. Times indicated below the graphs are the number of days after the initial implantation of the cells. All values represent mean \pm SEM. Data points represent values from independent eggs. Statistical test employed was Student's t-test. Values in **(B)** were normalized to respective DMSO average.

(C) Bar graph showing relative levels of *MCOLN1* mRNA in the UM-SCC-22A cells expressing *HRAS*^{WT} or *HRAS*^{G12V}. Values were normalized to *HRAS*^{WT} average and represent mean \pm SEM. Data points represent values from biological replicates. Statistical test employed was Student's t-test.

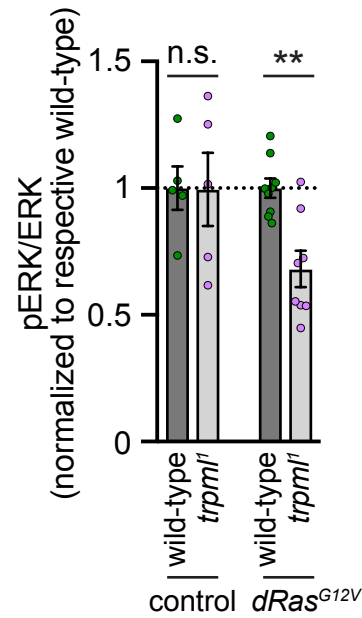
(D) Kaplan-Meier curves showing the survival of patients stratified on the basis of *MTM1* expression in BLCA and HNSC patients whose tumors were wild-type for *HRAS* (right) or carried oncogenic *HRAS* mutations (left).

(E) Kaplan-Meier curves showing the survival of patients stratified on the basis of *MCOLN1* expression in THCA patients whose tumors were wild-type for *HRAS* (right) or carried oncogenic *HRAS* mutations (left).

Statistical tests employed in **(D-E)** were Mantel-Cox log-rank test.



Appendix Figure S3. (A-B) Representative Western blots generated using extracts from MDCK cells expressing GFP-tagged oncogenic *HRAS* and controls treated with DMSO or ML-SI1 as indicated. The primary antibodies used were against GFP (A) and HRAS (B). (C) Bar graph showing quantification of the Western blots shown in (B). Values were normalized to respective DMSO average and represent mean \pm SEM. Data points represent values from biological replicates. Statistical test employed was Student's t-test. (D) Representative Western blots generated using extracts from HN31 cells exposed to the indicated perturbations. Primary antibodies used are indicated. (E) Bar graph showing quantification of the Western blots shown in (D). All values represent mean \pm SEM. Data points represent values from biological replicates. Statistical test employed was Student's t-test.



Appendix Figure S4. Bar graph showing pERK/ERK quantification of the Western blots shown in **Fig 5D**. Values represent mean±SEM. Data points represent values from biological replicates. Statistical tests employed were Student's t-test.